The Astrophysical Journal, 975:254 (16pp), 2024 November 10 https://doi.org/10.3847/1538-4357/ad7ea6

Adiabatic Mass Loss in Binary Stars. V. Effects of Metallicity and Nonconservative Mass Transfer—Application in High Mass X-Ray Binaries

Hongwei Ge[1,2,3,4], Christopher A. Tout[5], Xuefei Chen[1,2,3,4], Song Wang[6,7], Jianping Xiong[1,2,3], Lifu Zhang[1,4], Zhenwei Li[1,2,3,4], Qingzhong Liu[8], and Zhanwen Han[1,2,3,4]
[1] Yunnan Observatories, Chinese Academy of Sciences, Kunming, 650216, People's Republic of China; gehw@ynao.ac.cn; zhanwenhan@ynao.ac.cn
[2] Key Laboratory for Structure and Evolution of Celestial Objects, Chinese Academy of Sciences, Kunming 650216, People's Republic of China
[3] International Centre of Supernovae, Yunnan Key Laboratory, Kunming 650216, People's Republic of China
[4] University of Chinese Academy of Sciences, Beijing 100049, People's Republic of China
[5] Institute of Astronomy, The Observatories, University of Cambridge, Madingley Road, Cambridge, CB3 0HA, UK; cat@ast.cam.ac.uk
[6] Key Laboratory of Optical Astronomy, National Astronomical Observatories, Chinese Academy of Sciences, Beijing 100101, People's Republic of China
[7] Institute for Frontiers in Astronomy and Astrophysics, Beijing Normal University, Beijing 102206, People's Republic of China
[8] Key Laboratory of Dark Matter and Space Astronomy, Purple Mountain Observatory, Chinese Academy of Sciences, Nanjing, People's Republic of China
Received 2024 August 28; revised 2024 September 12; accepted 2024 September 13; published 2024 November 7

Abstract

Binary stars are responsible for many unusual astrophysical phenomena, including some important explosive cosmic events. The stability criteria for rapid mass transfer and common-envelope evolution are fundamental to binary star evolution. They determine the mass, mass ratio, and orbital distribution of systems such as X-ray binaries and merging gravitational-wave sources. We use our adiabatic mass-loss model to systematically survey metal-poor and solar-metallicity donor thresholds for dynamical timescale mass transfer. The critical mass ratios $q_{\rm ad}$ are systematically explored and the impact of metallicity and nonconservative mass transfer are studied. For metal-poor radiative-envelope donors, $q_{\rm ad}$ are smaller than those for solar-metallicity stars at the same evolutionary stage. However, $q_{\rm ad}$ do the opposite for convective-envelope donors. Nonconservative mass transfer significantly decreases $q_{\rm ad}$ for massive donors. This is because it matters how conservative mass transfer is during the thermal timescale phase immediately preceding a delayed dynamical mass transfer. We apply our theoretical predictions to observed high-mass X-ray binaries that have overfilled their Roche lobes and find a good agreement with their mass ratios. Our results can be applied to study individual binary objects or large samples of binary objects with binary population synthesis codes.

Unified Astronomy Thesaurus concepts: Binary stars (154); Stellar mass black holes (1611); Neutron stars (1108); High mass x-ray binary stars (733)

Materials only available in the online version of record: machine-readable tables

1. Introduction

Binary stars lie at the heart of many vital astrophysical phenomena (e.g., T. M. Tauris & E. P. J. van den Heuvel 2023). Different types of explosive cosmic events are produced by binary star objects, such as double black holes (BHs; e.g., I. Mandel & F. S. Broekgaarden 2022), double neutron stars (e.g., M. Gallegos-Garcia et al. 2023), double white dwarfs (DWDs, e.g., Z. Li & X. Chen 2024), type Ia supernovae (e.g., Z.-W. Liu et al. 2023), and X-ray binaries (e.g., T. M. Tauris & E. P. J. van den Heuvel 2023). The study of binary evolution brings new opportunities for insights into fundamental physics (e.g., P. Amaro-Seoane et al. 2023) such as testing general relativity, production of heavy chemical elements, and discovering new double compact systems in the next few decades. Despite the importance of binary evolution, there remain unsolved fundamental questions of particular importance, including mass transfer stability (R. F. Webbink 1984) and common envelope (CE) evolution (B. Paczynski 1976).

A series of recent studies have indicated that mass transfer in massive binary systems (H. Ge et al. 2015) and binaries with red/asymptotic giant branch (R/AGB) companions (H. Ge et al. 2020a, 2020b) are more stable than previously found. With these mass transfer thresholds as physical inputs, an isolated binary BH formation scenario consisting of a stable mass transfer during the second mass transfer phase (instead of CE) has been gaining popularity in the gravitational wave (GW) community (C. J. Neijssel et al. 2019). Besides the mass transfer physics, the supernova natal kicks (I. Mandel et al. 2021) are also critical for massive binary evolution. Hence, mass transfer is probably active in some systems in eccentric orbits. As for WD binaries, mostly formed from R/AGB progenitors, a first stable mass transfer plus a second CE channel may dominate the formation of DWDs (Z. Li et al. 2023). These objects are low-frequency GW sources detectable with Tianqin and LISA detectors (J. Luo et al. 2016; P. Amaro-Seoane et al. 2017).

Many observed stellar phenomena, including binaries, are dominated by metal-poor environments (H. Ge et al. 2023). Examples include blue stragglers (A. R. Sandage 1953), blue metal-poor stars (G. W. Preston & C. Sneden 2000), Galactic halo stars (H. Li et al. 2018), metal-poor thick disk stars (Y. Wu et al. 2021), ultraluminous X-ray sources (ULXs, L. Zampieri & T. P. Roberts 2009), partially stripped-envelope stars (J. Klencki et al. 2022), massive stellar-mass BHs and their mergers (J. S. Vink et al. 2021), and metal-poor inner Galactic stars (A. Ardern-Arentsen et al. 2024). Nonconservative mass transfer in binary evolution and

angular momentum loss play an important role in binary evolution (X. Chen et al. 2024). It may substantially impact predictions about the production rates of various transients, such as X-ray binaries and the progenitors of coalescing compact binaries (R. Willcox et al. 2023).

We extend our systematic studies of stars to metal-poor donors and nonconservative mass transfer. With our adiabatic mass-loss model, we only provide critical mass-ratio thresholds (H. Ge et al. 2010) assuming conservative mass transfer in the first place. However, the advantage is that the donor response to rapid mass transfer is independent of the binary orbital evolution. So our studies can easily resolve the nonconservative mass transfer cases. Our preliminary results have been included in binary population synthesis and applied to study objects such as DWDs (Z. Li et al. 2023). After the new thresholds have been applied, the results support the observational DWD merger rate distribution per Galaxy and the space density of DWDs in the Galaxy.

In Section 2, we describe methods to build an adiabatic mass-loss model and solve for the critical mass ratio under conservative and nonconservative mass transfer. Using massive $20\,M_{\odot}$ stars as examples, in Section 3, we study the impacts of metallicity and nonconservative mass transfer on the critical mass ratios for dynamical-timescale mass transfer in metal-poor $Z=0.001$ and solar-metallicity $Z=0.02$ stars.[9] In Section 4, we present our model grids and thresholds for unstable mass transfer. In Section 5, we collect observed high-mass X-ray binaries (HMXBs) with known binary parameters and compare mass ratios and orbital periods with our theoretical predictions. In Sections 6 and 7, we discuss and summarize our systematic studies of the thresholds for dynamical-timescale mass transfer.

2. Methods

We use our adiabatic mass-loss model to study the responses of donor stars undergoing rapid mass transfer. H. Ge et al. (2010) described the detailed method and numerical implementation. The stellar evolution code is updated and extended by H. Ge et al. (2015, 2020a, 2023) and is based on the Cambridge Stars Code (O. R. Pols et al. 1995) originally developed by P. P. Eggleton (1971).

We extend our previous studies of dynamical-timescale mass transfer thresholds for nonconservative cases. This extension is essential for the delayed dynamical instability of donor stars with a deep radiative envelope. We first recall the key points to calculate the critical initial mass ratio $q_{\rm ad}$ for the dynamical-timescale mass transfer. The classical method (R. F. Webbink 1985) is to compare the slope of the mass–radius relation of both the stellar radius R and the Roche radius $R_{\rm L}$, such as Equations (2)–(11) of H. Ge et al. (2010). The slopes are expressed by the so-called mass–radius exponents,

$$\zeta_{\rm ad}\equiv\left(\frac{d\log R}{d\log M}\right)_{\rm ad}, \tag{1}$$

and

$$\zeta_{\rm L}\equiv\frac{d\log R_{\rm L}}{d\log M}, \tag{2}$$

where $\zeta_{\rm ad}<\zeta_{\rm L}$ implies instability on a dynamical-timescale mass transfer and $\zeta_{\rm ad}\geqslant\zeta_{\rm L}$ implies stable mass transfer. However, runaway mass transfer increases gradually and some donors may have a loose and low-density envelope. So, instead of using the surface radius R of the donor star, we use an inner radius $R_{\rm KH}$ to calculate the mass–radius exponent, $\zeta_{\rm ad}^{\rm KH}=d\ln R_{\rm KH}/d\ln M|_{\rm ad}$. This inner radius $R_{\rm KH}$ determines when the mass-loss rate $\dot{M}$ (see A9 of H. Ge et al. 2010) reaches a thermal timescale rate $\dot{M}_{\rm KH}=M/t_{\rm KH}$.

We assume a donor star overfills its Roche lobe at some initial mass and radius—the nth model from evolutionary sequences counting from the zero-age main-sequence (ZAMS). The critical initial mass ratio $q_{\rm i}\equiv M_{\rm donor}/M_{\rm accretor}=M_{\rm d}/M_{\rm a}$ for dynamical-timescale mass transfer is to be determined. We define a mass function $\mu=M_{\rm d}/(M_{\rm d}+M_{\rm a})=q/(1+q)$ which lies between 0 and 1. For the adiabatic mass-loss sequences, we enumerate models by $b\in\{1,\ 2,\ldots,B\}$. Initially, $b=1$, the initial mass is $M_{\rm i}$ and radius $R_{\rm i}$. The initial separation $A_{\rm i}$ is such that $R_{\rm i}=R_{\rm L}$, the Roche-lobe radius of the donor. For model b, the remaining total mass M_b and the inner radius $R_{\rm KH}^b$ are found by our adiabatic mass loss (H. Ge et al. 2010). The mass–radius exponent $\zeta_{\rm ad}^{\rm KH}$ can thus be found with models $b-1$ and b. It is independent of whether the mass transfer is conservative or not. To find the critical initial mass ratio, we need to know the mass–radius exponent $\zeta_{\rm L}$, which depends on how conservative the mass transfer is.

The inner Lagrangian Roche-lobe radius $R_{\rm L}$ of the donor (P. P. Eggleton 1983) can be expressed by

$$\frac{R_{\rm L}}{A}=r_{\rm L}(q)=\frac{0.49q^{2/3}}{0.6q^{2/3}+\ln(1+q^{1/3})}. \tag{3}$$

Differentiating Equation (3) we have

$$\frac{d\ln r_{\rm L}}{d\ln q}=\frac{1}{3}\left[\frac{2\ln(1+q^{1/3})-q^{1/3}/(1+q^{1/3})}{0.6q^{2/3}+\ln(1+q^{1/3})}\right]. \tag{4}$$

According to H. Ge et al. (2020b), the outer Lagrangian Roche-lobe radius of the donor $R_{\rm L}^{\rm out}=r_{\rm L}^{\rm out}(q)A$ can be found from

$$r_{\rm L}^{\rm out}(q)=r_{\rm L}(q)+\left[0.179+0.01\left(\frac{q}{1+q}\right)\right]\times\left(\frac{q}{1+q}\right)^{0.625}\quad\text{for } q\leqslant 1, \tag{5}$$

and

$$r_{\rm L}^{\rm out}(q)=r_{\rm L}(q)+\left[0.179+0.01\left(\frac{q}{1+q}\right)-0.025\left(\frac{q-1}{q}\right)\right]\left(\frac{q}{1+q}\right)^{0.625}q^{-0.74}\text{for } q\geqslant 1. \tag{6}$$

In terms of Lagrangian surfaces, the physical radius of the donor outer lobe is $R_{\rm L_3}$ for $q>1$ and $R_{\rm L_2}$ for $q<1$.

For conserved mass and angular momentum, H. Ge et al. (2023) found

$$\frac{R_{\rm L}(\mu_b)}{R_{\rm i}}=\frac{r_{\rm L}(\mu_b)}{r_{\rm L}(\mu_{\rm i})}\left(\frac{\mu_{\rm i}}{\mu_b}\right)^2\left(\frac{1-\mu_{\rm i}}{1-\mu_b}\right)^2, \tag{7}$$

[9] Recent studies indicate a lower metallicity in the solar atmosphere (e.g., M. Asplund et al. 2009).

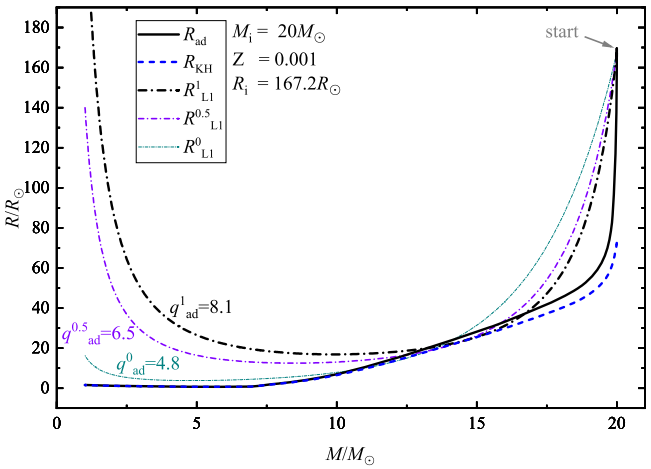

Figure 1. Example critical mass ratios q_{ad} for conservative and nonconservative mass transfer. The initial parameters are labeled. The black solid line marks the radius response during the adiabatic mass-loss process. The blue dashed line is the inner radius R_{KH}. The dashed–dotted lines are the Roche-lobe radii under conservative (black), semiconservative (violet), and fully nonconservative (cyan) mass transfer.

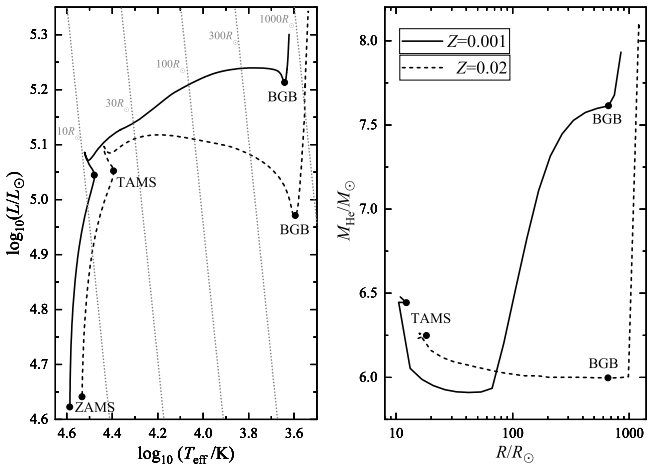

Figure 2. The left-hand panel shows the evolution for $20\,M_\odot$ stars with different metallicities in the Hertzsprung–Russell diagram. The right-hand panel presents their helium core masses M_{He}, where core hydrogen mass fraction first reaches 0.15, as a function of their radii. Solid and dashed lines are stars with metallicities of $Z = 0.001$ and $Z = 0.02$.

where $\mu_b = \mu_i M_b/M_i$ and $\mu = q/(1 + q)$. For nonconservative mass transfer, a fraction α of the total mass lost by the donor is transferred to its companion. So, a fraction $1 - \alpha$ of the donor mass lost carries away the donor's specific angular momentum. We further suppose that a faction β of the transferred mass is accreted so that a faction $(1 - \beta)$ of the transferred mass is ejected from the accretor with γ times its specific angular momentum. So, for mass-loss model b, the mass ratio

$$q = \frac{M_b}{M_i/q_i + \alpha\beta(M_i - M_b)}, \tag{8}$$

and the separation varies as

$$\frac{A_b}{A_{b-1}} = 1 + \frac{2(M_{b-1} - M_b)}{M_b} \times \left[\alpha(1 - q\beta) - \frac{q}{1 + q}(\gamma q + 0.5)(1 - \alpha\beta)\right]. \tag{9}$$

When mass is only lost from the accretor and carries away its specific angular momentum, we have $\alpha = 1$ and $\gamma = 1$. We set $\beta = 1$ (fully conservative), 0.5 (nonconservative), and 0 (fully nonconservative) in this study. Starting from an initial guess, $\mu_i = 0.5$, we use a bisection method to calculate the initial mass function, μ_b, satisfying both $R^b_L = R^b_{KH}$ and $\zeta^b_L = \zeta^b_{KH}$. By tracing $b = 1$ to $b = B$ for the whole adiabatic mass-loss process, we can get the minimum value of μ_{min}. So, the critical initial mass ratio is calculated finally with $q_{ad} = \mu_{min}/(1 - \mu_{min})$.

Similar to H. Ge et al. (2015, 2020a), we build parallel donor star sequences with isentropic envelopes alongside standard donor stars with standard convective envelopes. In such stars, convective envelopes are replaced by fully isentropic envelopes. With this, the limitations of an adiabatic approximation in a thin layer just below the photosphere are overcome. For such stars we calculate critical initial mass ratios $\tilde{q}_{ad}$.

We demonstrate our method for a metal-poor star of $20\,M_\odot$ and $167.2\,R_\odot$ in Figure 1. The Roche-lobe radius becomes much smaller when the mass transfer is more nonconservative. This allows a shallower descent of Roche-lobe radius for nonconservative mass transfer. Hence, critical mass ratios q_{ad} become smaller rather than larger for nonconservative mass transfer.

3. Massive Stars of $20\,M_\odot$ with Varying Metallicities

We choose $20\,M_\odot$ massive donor stars as examples to demonstrate the impacts of both metallicity and mass transfer physics. A metal-poor star behaves as if it is more massive than a similar mass solar-metallicity star (Figure 2). Such behavior is similar for intermediate-mass donor stars (H. Ge et al. 2023). A metal-poor massive star has a slightly higher central temperature T_c and develops a larger helium core mass M_{He} at the end of the main sequence (MS). However, the convective core moves off-center and shrinks for a while until helium ignites in the center, after which M_{He} increases to exceed that of a $Z = 0.02$ star of the same radius (Figure 2).

The stellar radius R can be used to represent the evolutionary state of a star because it determines when Roche-lobe overflow (RLOF) begins. The initial orbital period P_{orb}, or separation A, of a binary system only weakly depends on mass ratio but strongly depends on donor radius (H. Ge et al. 2015, Section 2). Metal-poor ($Z = 0.001$) massive stars have a longer core hydrogen burning lifetime (e.g., G. Schaller et al. 1992) and smaller radii R than those of same mass but $Z = 0.02$ star (Figure 3).

H. Ge et al. (2020a) presented critical mass ratios q_{ad} for $0.1 \leqslant M/M_\odot \leqslant 100$ stars with solar metallicity. They confirmed that donor stars with radiative and convective envelopes behave differently during adiabatic mass loss. Meanwhile, on the MS, Hertzsprung gap (HG), and just before the base of the giant branch (BGB), intermediate-mass (H. Ge et al. 2020a, 2023) and massive stars (H. Ge et al. 2020a) have a similar structure, including an outer radiative envelope. Although the massive star is complicated by multiple convection zones, its radiative envelope dominates behavior under adiabatic mass loss. Such donor stars are predicted to undergo delayed dynamical instability (M. S. Hjellming & R. F. Webbink 1987; H. Ge et al. 2010) if the initial mass ratio q_i is larger than q_{ad}. We find that the critical mass ratios q_{ad} and

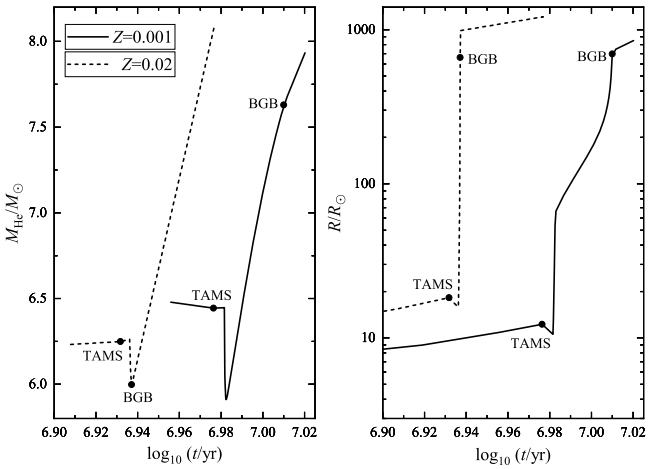

Figure 3. The impact of metallicity on helium core mass M_{He} (left-hand panel) and the radius R (right-hand panel) as functions of a 20 $M_\odot$ star's age. Solid and dashed lines are $Z = 0.001$ and $Z = 0.02$ stars.

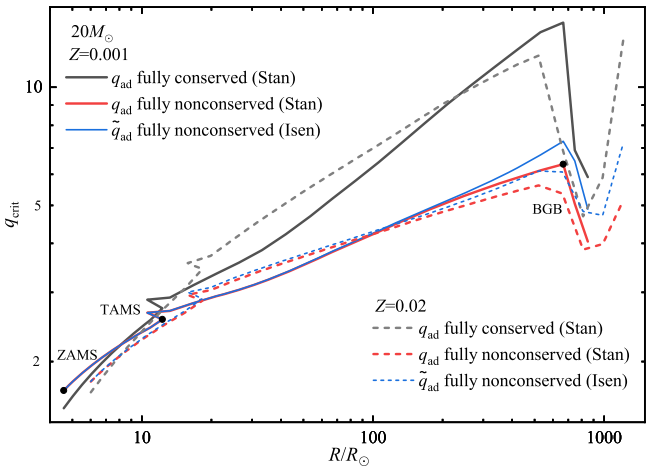

Figure 4. Critical initial mass ratios q_{ad} as functions of stellar radius for 20 $M_\odot$ models. The solid and dashed lines correspond to $Z = 0.001$ and $Z = 0.02$ stellar models. Red and blue lines correspond to models with standard mixing-length envelopes q_{ad} and artificially isentropic convective envelopes $\tilde{q}_{ad}$ for fully nonconservative mass transfer. Gray lines show stellar models with standard envelopes q_{ad} for fully conservative mass transfer.

$\tilde{q}_{ad}$ increase with the radius as the star evolves from the ZAMS to the BGB (Figure 4). The convection envelope dominates once a massive star becomes a red giant branch (GB) or a red supergiant (RSG). However, the thermal timescale becomes very short for convective envelope giants. So, the threshold for thermal timescale mass loss through the outer-Lagrangian point q_{th}^{Lout} is likely to become stricter compared to q_{ad} (H. Ge et al. 2020b). In other words, binary systems, containing such kind of donors, with initial mass ratios $q_{th}^{Lout} < q_i < q_{ad}$ may enter a common envelope phase.

After the mass of a star, its metallicity is the second most important parameter for its structure and evolution. However, metallicity seems only to shift the critical mass ratios q_{ad} of massive stars (same mass) in radius (Figure 4). The critical mass ratio trend looks quite similar for 20 $M_\odot$ massive stars of different metallicities. As we described in the previous section, the donor response to adiabatic mass loss is independent of the orbital evolution of a rapidly mass-transferring binary system. However, how much mass and angular momentum is lost from

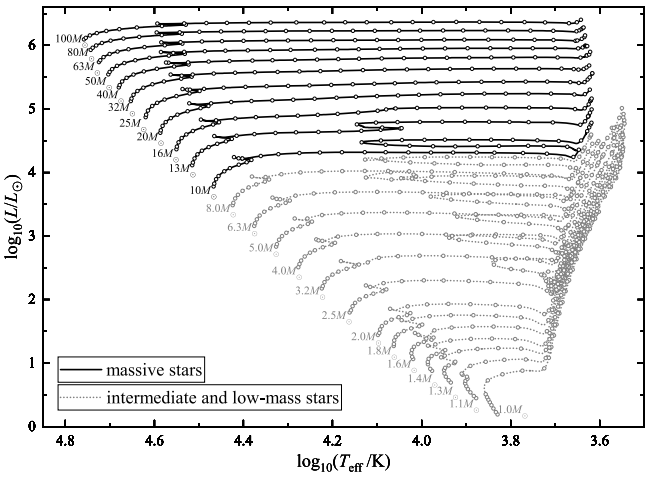

Figure 5. The evolution of metal-poor ($Z = 0.001$) stars. Black solid lines indicate massive donor stars, while gray dotted lines are low- and intermediate-mass stars. Some of the intermediate and low-mass stars were studied by H. Ge et al. (2023). We also extend the donor spaces in this study. Open circles are placed at $\Delta \log_{10} R = 0.1$ from the ZAMS.

the binary system significantly affects the Roche lobes of two components and the orbital period. So, before entering a delayed dynamical instability, conservative and nonconservative mass transfer alter the initial critical mass ratio q_{ad} dramatically (Figure 4). The critical mass ratios of evolved donors of different metallicities decrease significantly for nonconservative mass transfer. These reduced critical initial mass ratios are caused by a longer thermal timescale mass transfer before entering the delayed unstable process. Surprisingly, the differences between fully nonconservative q_{ad} (red) and $\tilde{q}_{ad}$ (blue) along to metallicity are not significant (Figure 4).

4. Model Grids and Thresholds for Unstable Mass Transfer

Previously, H. Ge et al. (2020a) studied the adiabatic responses of Population I ($Z = 0.02$) stars spanning a full range of stellar mass (0.10–100 $M_\odot$) and all evolutionary stages. H. Ge et al. (2023) extended the study to metal-poor donor stars. Here, we also include nonconservative mass loss. This is essential for binary population synthesis studies of compact binaries with WD, neutron star (NS), or BH companions.

We cover a mass range from 1 to 100 $M_\odot$ (Figure 5). We present the initial physical properties of different donor stars and their thresholds for dynamical-timescale mass transfer in the Appendix and online. Tables A1 and A2 list interior and global physical properties of metal-poor donor stars. We only provide a 20 $M_\odot$ stellar sequence in this print version but list all the data in a machine-readable version. Table A3 lists thresholds for conservative and nonconservative dynamical-timescale mass transfer for metal-poor stars. Table A4 extends the thresholds for nonconservative dynamical-timescale mass transfer in solar-metallicity stars (from 0.1 to 100 $M_\odot$).

We plot the critical mass ratios q_{ad} of metal-poor intermediate-mass 5 $M_\odot$ and massive from 10 to 100 $M_\odot$ stars in Figures 6 and 7. During core-helium burning, the critical mass ratios increase dramatically because a deep convective envelope is replaced by a thick radiative envelope. Massive donors show similar trends to the 20 $M_\odot$ stars. The critical mass ratio q_{ad} increases the evolution of the donor until a convective envelope appears (Figure 7).

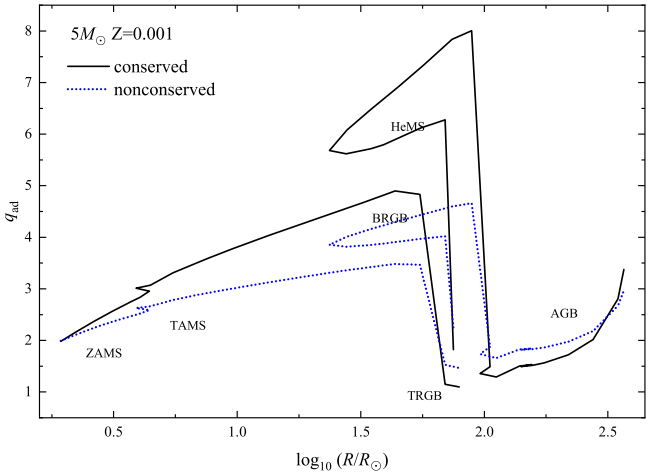

Figure 6. Critical mass ratios q_{ad} as functions of stellar radius for 5 $M_\odot$ stars. The solid (black) and dotted (blue) lines correspond to models of fully conservative and nonconservative mass transfer.

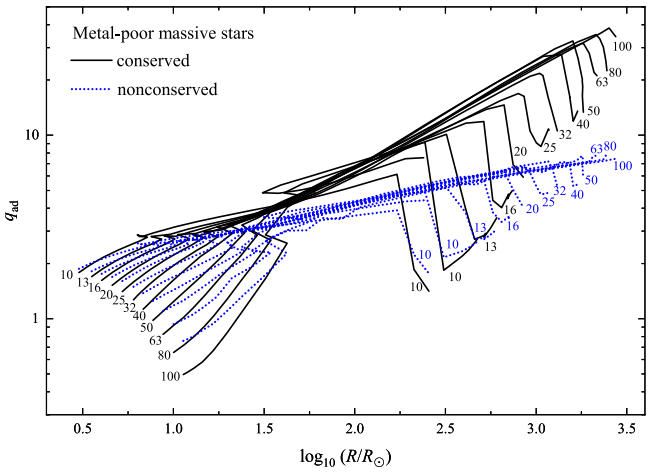

Figure 7. Critical mass ratios q_{ad} as functions of stellar radius for metal-poor massive stars. The masses in units of $M_\odot$ are labeled for each track. The solid (black) and dotted (blue) lines correspond to models of fully conservative and nonconservative mass transfer.

5. High-mass X-Ray Binaries

A HMXB is generally defined as a binary star system consisting of an NS or a BH accreting matter from a high-mass ($M \gtrsim 10 M_\odot$) stellar companion (E. P. J. van den Heuvel & J. Heise 1972; A. Tutukov & L. Yungelson 1973). Over 400 HMXBs have been found in the Milk Way (F. Fortin et al. 2023), the Large (V. Antoniou & A. Zezas 2016) and Small (F. Haberl & R. Sturm 2016) Magellanic Clouds, and nearby galaxies (B. D. Lehmer et al. 2021). The donor stars in HMXBs are dominated by supergiant (Sg) O/B stars or Be stars (F. Fornasini et al. 2023), and there are a few HMXBs with Wolf–Reyet donors or near naked helium stars. Other HMXBs include gamma-ray binaries that are dominated by gamma-rays above 1 Mev rather than X-rays and ultraluminous, $L_X > 1 \times 10^{39}$ erg s^{-1}, sources. HMXBs are important in modern astrophysics, e.g., first generations of HMXBs may provide X-ray heating to intergalactic gas and impact the onset and duration of Epoch of Reionization (M. Jeon et al. 2014), and therefore understanding the formation and evolution of

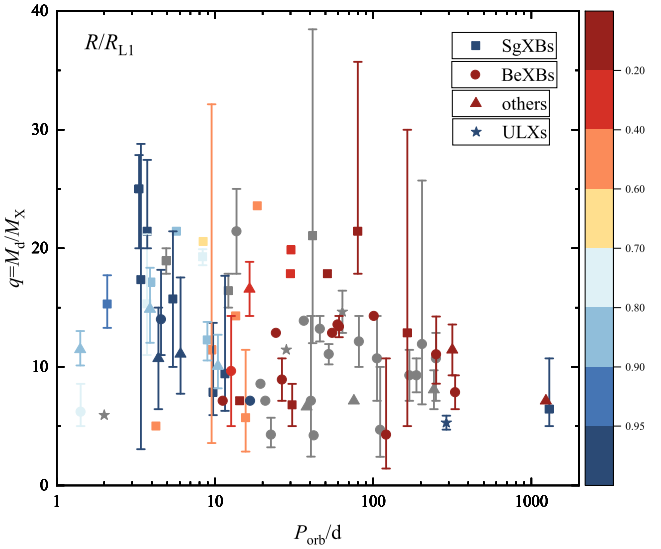

Figure 8. The ratio of donor radius R to Roche-lobe radius R_L of 82 HMXBs in Table 1 on a mass-ratio against the orbital-period diagram. Symbols represent the types of HMXBs in the Table. Colors (gray means unknown) show the ratio of donor radius to its Roche-lobe radius.

HMXBs provides important insights into one of the primary formation channels of GW sources (F. Fornasini et al. 2023).

Updated catalogs of HMXBs have recently been provided by M. Neumann et al. (2023) and F. Fortin et al. (2023). New HMXBs, including ULXs (D. Misra et al. 2020), have been found since the widely used catalog of Q. Z. Liu et al. (2006). From the observed HMXBs, we select 82 objects with known orbital information. We gather their orbital periods P_{orb}, compact companion masses M_X, donor masses M_d, peak X-ray luminosities L_X, and eccentricities e along with other useful information in Table 1.

We further select HMXBs undergoing stable mass transfer in circular orbits to compare our theoretical results. Unlike low and intermediate-mass X-ray binaries, most HMXBs are wind mass-transferring systems. So, the mass ratio $q = M_d/M_X$ of HMXBs can be large, i.e., over 20 (Figures 8 and 9). These are much larger than the mass ratios of intermediate-mass X-ray binaries, which reach $q_{max} \approx 6$ (Figure 17 and Table 3 of H. Ge et al. 2023) that are undergoing stable RLOF. From Figure 8, we see that most of the relatively long orbital-period ($P_{orb} > 10$ days) HMXBs have low ratios of donor radius to Roche-lobe radius. On the other hand, at relatively short orbital periods ($P_{orb} < 10$ days) most HMXBs are close to or undergoing stable RLOF.

Similarly, we find that relatively long orbital-period ($P_{orb} > 10$ days) HMXBs can have a moderately ($e > 0.35$) to highly eccentric orbits (Figure 9). On the contrary, short-period HMXBs ($P_{orb} < 10$ days) are generally in low ($e < 0.35$) eccentricity orbits. When the progenitor of the accreting NS or BH explodes as a supernova, there is likely a natal kick caused by spatially asymmetric mass loss or neutrino emission (S. E. Woosley 1987). Such natal kicks can change the eccentricity and the final separation, and can even unbind otherwise runaway binary systems (B. P. Flannery & E. P. J. van den Heuvel 1975; J. G. Hills 1983). Here, we select HMXBs with a low eccentricity ($e < 0.35$) and a high filling degree ($R/R_L > 0.95$) on the demands that they are closest to stable RLOF.

Table 1
Observed HMXBs with Known Masses and Orbital Periods

Name	X-ray Type	$P_{\rm orb}$ (days)	Peak $L_{\rm X}$ (erg s^{-1})	$q = M_{\rm d}/M_{\rm X}$	$M_{\rm X}$ ($M_\odot$)	SpType[a]	$M_{\rm d}$ ($M_\odot$)	e	$R_{\rm d}$ ($R_\odot$)	$R_{\rm L}$ ($R_\odot$)	References
				SgXBs							
4U 1954+31	SG	1296.64	⋯	$6.43^{+4.29}_{-1.43}$	1.40	M4I	$9.00^{+6.00}_{-2.00}$	0.500	586.0	591.9	(1)
IGR J11215-5952	SG, XT	164.60	5.10E+36	$12.86^{+17.14}_{-7.86}$	1.40	B0.5Ia	$18.00^{+24.00}_{-11.00}$	0.800	28.0	202.9	(2–4)
IGR J16318-4848	RS, SG	80.00	4.00E+36	$21.43^{+14.29}_{-3.57}$	1.40	B0-5sgBe	$30.00^{+20.00}_{-5.00}$	⋯	20.4	156.3	(5, 6)
IGR J17391-3021	SG, XT	51.47	1.00E+36	17.86	1.40	O8Iab(f)	25.00	<0.800	18.8	107.8	(2, 7, 8)
GX 301-2	CL, SG, XP, XT	41.50	3.00E+37	$21.05^{+17.41}_{-9.05}$	$1.90^{+0.60}_{-0.60}$	B1.5Ia	$40.00^{+10.00}_{-10.00}$	0.470	⋯	110.9	(9–12)
IGR J05007-7047	SG	30.77	9.00E+36	$6.79^{+1.79}_{-1.79}$	1.40	B2III	$9.50^{+2.50}_{-2.50}$	⋯	4.8	50.1	(13)
IGR J16465-4507	SG, XP, XT	30.32	6.80E+36	19.86	1.40	B0.5-1Ib	27.80	⋯	22.1	79.3	(2, 14)
SAX J1818.6-1703	SG, XT	30.00	8.00E+35	17.86	1.40	B0.5Iab	25.00	0.350	30.0	75.2	(15, 16)
IGR J18483-0311	SG, XT	18.55	7.80E+36	23.57	1.40	B0.5-1Iab	33.00	0.40-0.68	33.8	61.4	(2, 4, 17)
IGR J00370+6122	SG	15.66	3.00E+36	$5.71^{+5.71}_{-2.86}$	1.40	BN0.7Ib	$8.00^{+8.00}_{-4.00}$	0.560	17.0	29.6	(3, 18, 19)
1E 1145.1-6141	RS, SG, XP	14.37	4.70E+37	7.14	1.40	B2Iae	10.00	0.200	5.0	30.8	(4, 20)
IGR J19140+0951	SG	13.56	3.00E+35	14.29	1.40	B0.5Ia	20.00	⋯	20.0	40.2	(2, 21)
IGR J17544-2619	SG, XT	12.17	5.30E+36	$16.43^{+1.43}_{-1.43}$	1.40	O9Ib	$23.00^{+2.00}_{-2.00}$	0.440	⋯	39.8	(4, 22–25)
2S 0114+650	CL, SG, XP	11.60	1.20E+37	$9.41^{+8.27}_{-3.12}$	$1.70^{+0.10}_{-0.50}$	B1Iae	$16.00^{+5.00}_{-5.00}$	0.160	37.0	32.2	(2, 4, 26, 27)
IGR J17252-3616	EB, SG, XP	9.74	1.60E+37	$7.85^{+5.85}_{-1.92}$	$1.91^{+0.45}_{-0.45}$	B0-B1Ia	$15.00^{+5.00}_{-1.00}$	<0.190	29.0	27.5	(2, 28)
4U 2206+54	BE, CL, QPO, SG, XP	9.57	5.50E+35	11.43	1.40	O9.5Vep	16.00	0.150	7.3	28.9	(3, 4, 29)
IGR J08408-4503	SG, XT	9.54	6.00E+36	$11.43^{+20.71}_{-7.86}$	1.40	O8.5Ib-II(f)p	$16.00^{+29.00}_{-11.00}$	0.630	17.0	28.9	(3, 30)
Vela X-1	CL, EB, RS, SG, XP	8.96	1.00E+37	$12.26^{+1.52}_{-1.73}$	$2.12^{+0.16}_{-0.16}$	B0.5Ib	$26.00^{+1.00}_{-2.00}$	0.090	29.0	32.8	(4, 28, 31, 32)
IGR J17354-3255	SG, XT	8.45	2.60E+36	20.57	1.40	O9.5Iab	28.80	0.200	22.4	34.3	(2, 33)
4U 1907+09	CL, HT, SG, XP, XT	8.38	4.80E+36	$19.29^{+0.64}_{-0.71}$	1.40	O8-9Ia	$27.00^{+0.90}_{-1.00}$	0.280	26.2	33.2	(4, 34, 35)
IGR J18450-0435	SG, XT	5.72	8.00E+36	$21.43^{+0.00}_{-0.00}$	1.40	O9.5I	30.00^{+}_{-}	<0.370	23.0	26.9	(36)
IGR J18214-1318	SG	5.42	5.00E+36	$15.71^{+5.71}_{-5.71}$	1.40	B0V-O9I	$22.00^{+8.00}_{-8.00}$	0.170	22.0	22.8	(37, 38)
IGR J17544-2619	CL, SG, XT	4.93	3.00E+38	$18.93^{+1.07}_{-1.07}$	1.40	O9Ib	$26.50^{+1.50}_{-1.50}$	<0.400	⋯	23.1	(22, 39)
IGR J18027-2016	SG, CL, EB, QPO, XP, XT	4.57	1.30E+37	$14.01^{+4.17}_{-3.02}$	$1.57^{+0.25}_{-0.25}$	B1Ib	$22.00^{+2.00}_{-2.00}$	0.200	20.0	20.1	(2, 4, 28, 40)
IGR J16393-4643	CL, SG, XB, XP, EB	4.24	⋯	5.00	1.40	BIV-V(OB)	7.00	⋯	6.3	11.7	(40, 41)
IGR J16195-4945	SG	3.95	⋯	17.14	1.40	ON9.7Iab	24.00	⋯	17.0	19.1	(42)
IGR J16418-4532	SG, XT, EB	3.74	2.10E+37	$21.43^{+6.03}_{-1.43}$	1.40	O7.5Ia	$30.00^{+8.44}_{-2.00}$	⋯	21.7	20.3	(2, 4, 41)
4U 1538-52	CL, EB, SG, XP	3.73	9.00E+36	$15.31^{+5.87}_{-4.31}$	$1.30^{+0.20}_{-0.20}$	B0Iab	$19.90^{+3.40}_{-3.40}$	0.180	13.0	17.1	(11, 28, 43)
4U 1700-377	EB, RS, SG	3.41	2.20E+36	$17.35^{+11.46}_{-14.29}$	$1.96^{+0.19}_{-0.19}$	O6Iafcp	$34.00^{+17.00}_{-28.00}$	<0.220	19.0	19.5	(3, 28)
IGR J16479-4514	SG, XT, EB	3.32	1.09E+34	$25.00^{+2.86}_{-5.00}$	1.40	O7I	$35.00^{+4.00}_{-7.00}$	⋯	20.5	20.0	(41)
Cen X-3	CL, EB, QPO, SG, XP	2.09	5.40E+37	$15.29^{+2.44}_{-2.00}$	$1.57^{+0.16}_{-0.16}$	O6.5II-III	$24.00^{+1.00}_{-1.00}$	<0.002	11.4	12.4	(11, 28)
				BeXBs							
RX J0146.9+6121	BE	330.00	1.10E+35	$7.86^{+1.43}_{-1.43}$	1.40	B1III-Ve	$11.00^{+2.00}_{-2.00}$	⋯	7.0	259.8	(44)
4U 0352+30	BE, CL, XP	250.30	6.30E+34	$11.06^{+3.19}_{-2.48}$	1.40	B0Ve	$15.49^{+4.46}_{-3.47}$	0.110	6.4	251.2	(2, 4, 45)
GRO J1008-57	BE, CL, HT, XP, XT	249.50	1.00E+38	$10.71^{+2.14}_{-3.57}$	1.40	B0IIIVe	$15.00^{+3.00}_{-5.00}$	0.680	⋯	247.2	(11, 46, 47)
gam Cas	BE, Gcas, RS	203.59	⋯	$11.92^{+13.79}_{-5.08}$	$1.30^{+0.60}_{-0.60}$	B0.5IVpe	$15.50^{+2.50}_{-2.50}$	0.260	⋯	220.7	(48)
4U 1145-619	BE, XP, XT	187.50	1.90E+35	$9.29^{+1.43}_{-1.43}$	1.40	B0.2III	$13.00^{+2.00}_{-2.00}$	⋯	⋯	191.9	(4, 49–51)
XTE J1946+274	BE, CL, XP, XT	169.20	5.00E+37	$9.29^{+2.14}_{-2.14}$	1.40	B0-1IV-Ve	$13.00^{+3.00}_{-3.00}$	0.330	⋯	179.2	(52)
IGR J11305-6256	BE	120.83	1.00E+35	$4.29^{+6.43}_{-2.86}$	1.40	B0IIIne	$6.00^{+9.00}_{-4.00}$	⋯	6.0	101.7	(3, 53)
1A 0535+262	BE, CL, HT, QPO, RS, XP, XT	110.60	4.90E+37	$4.69^{+5.31}_{-2.27}$	$1.60^{+0.60}_{-0.60}$	O9.7IIIe	$7.50^{+2.50}_{-2.50}$	0.350	⋯	104.3	(11, 51)
GS 0834-430	BE, XP, XT	105.80	1.10E+37	$10.71^{+3.57}_{-3.57}$	1.40	B0-2III-Ve	$15.00^{+5.00}_{-5.00}$	0.120	⋯	139.5	(50, 54)

Table 1
(Continued)

Name	X-ray Type	P_{orb} (days)	Peak L_X (erg s^{-1})	$q = M_d/M_X$	M_X ($M_\odot$)	SpType[a]	M_d ($M_\odot$)	e	R_d ($R_\odot$)	R_L ($R_\odot$)	References
MXB 0656-072	BE, CL, QPO, XP, XT	101.00	6.60E+36	14.29	1.40	O9.7Ve	20.00	0.400	15.0	153.4	(55)
LS 992	BE, XP, XT	81.30	2.30E+36	$12.14^{+2.14}_{-2.14}$	1.40	B0.2IVe	$17.00^{+3.00}_{-3.00}$	⋯	⋯	123.7	(4, 50, 56)
LS 1698	BE, XP, XT	60.90	4.50E+35	$13.39^{+0.89}_{-0.89}$	1.40	B0V-IIIe	$18.75^{+1.25}_{-1.25}$	⋯	11.2	106.4	(57, 58)
SGR 0755-2933	BE	59.52	1.00E+34	13.57	1.40	B0Ve	19.00	0.060	12.6	105.4	(4, 59)
GRO J2058+42	BE, CL, XP, XT	55.03	5.60E+37	12.86	1.40	O9.5-B0IV-Ve	18.00	0.600	10.0	97.7	(60)
IGR J11435-6109	BE, XP, XT	52.46	2.10E+36	$11.07^{+0.86}_{-0.86}$	1.40	B0.5Ve	$15.50^{+1.20}_{-1.20}$	⋯	⋯	88.7	(4, 61)
EXO 2030+375	BE, CL, XP, XT	46.02	1.00E+38	$13.21^{+1.07}_{-1.07}$	1.40	B0Ve	$18.50^{+1.50}_{-1.50}$	0.410	⋯	87.8	(62, 63)
2S 1417-624	BE, XP, XT	42.12	8.00E+36	4.21	1.40	B1Ve	>5.9	0.446	⋯	50.0	(50, 64)
KS 1947+300	BE, CL, HT, XP, XT	40.42	2.00E+37	$7.14^{+7.14}_{-4.71}$	1.40	B0Ve	$10.00^{+10.00}_{-6.60}$	0.030	⋯	61.4	(65, 66)
V0332+53	BE, CL, HT, QPO, XP, XT	36.50	3.75E+38	13.89	1.44	O8-9Ve	>20	0.417	⋯	77.6	(11, 67)
LS I +61 303	BE, GP, RS	26.50	⋯	$8.93^{+1.79}_{-1.79}$	1.40	B0Ve	$12.50^{+2.50}_{-2.50}$	0.540	7.0	51.2	(68)
4U 0115+63	BE, CL, HT, QPO, XB, XP, XT	24.30	1.02E+38	12.86	1.40	B0.2Ve	18.00	0.340	8.0	56.7	(69, 70)
4U 1901+03	BE, CL, XP, XT	22.58	1.10E+38	$4.29^{+1.43}_{-1.07}$	1.40	B8-9 IVe	$6.00^{+2.00}_{-1.50}$	0.036	⋯	33.2	(71)
Cep X-4	BE, CL, HT, XP, XT	20.85	1.40E+36	7.14	1.40	B1-B2Ve	10.00	⋯	⋯	39.5	(11, 72)
XTE J0421+560	BE, SG, XT	19.41	3.00E+38	8.57	1.40	B1/2I[e]	>12	0.620	⋯	40.8	(73, 74)
Cir X-1	BE?	16.68	1.00E+38	7.14	1.40	B5-A0I	10.00	0.450	40.0	34.0	(75, 76)
IGR J14059-6116	GP, BE	13.71	5.60E+33	$21.43^{+3.57}_{-3.57}$	1.40	O6.5III	$30.00^{+5.00}_{-5.00}$	⋯	⋯	48.2	(77, 78)
SAX J2103.5 + 4545	BE, XP, XT	12.68	8.40E+36	$9.64^{+4.64}_{-4.64}$	1.40	B0Ve	$13.50^{+6.50}_{-6.50}$	0.400	8.0	32.4	(4, 79, 80)
PSR J0635 + 0533	BE, XP	11.20	2.76E+33	7.14	1.40	B1IIIe-B2Ve	10.00	0.290	⋯	26.1	(4, 81)
RX J0050.7-7316	BE	1.42	1.00E+36	$6.21^{+2.36}_{-1.21}$	1.40	B	$8.70^{+3.30}_{-1.70}$	⋯	4.3	6.2	(41, 82)
					Other XBs						
PSR B1259-63	GP	1236.72	8.00E+35	7.14	1.40	B2e/O9.5Ve	10.00	0.870	6.0	600.9	(2, 83, 84)
HESS J0632 + 057	GP	316.80	⋯	$11.43^{+2.14}_{-2.14}$	1.40	B0Vpe	$16.00^{+3.00}_{-3.00}$	0.620	8.0	298.2	(85, 86)
2S 1845-024	XP, XT	242.18	3.00E+37	$8.07^{+1.64}_{-1.64}$	1.40	OB	$11.30^{+2.30}_{-2.30}$	0.880	⋯	213.9	(4, 87, 88)
XTE J1543-568	XP, XT	75.56	1.20E+37	7.14	1.40	Be?	>10	0.030	⋯	93.2	(50, 89)
XTE J1859 + 083	XP, XT	37.97	1.00E+36	6.64	1.40	B0-2Ve	>9.3	0.127	⋯	57.1	(90–92)
1FGL J1018.6-5856	GP	16.55	⋯	$16.57^{+2.29}_{-2.29}$	1.40	O6V((f))	$23.20^{+3.20}_{-3.20}$	0.530	10.0	49.0	(51, 93)
OAO 1657-415	CL, EB, XP	10.45	2.00E+37	$10.06^{+2.65}_{-1.87}$	$1.74^{+0.30}_{-0.30}$	B0-6sg	$17.50^{+0.80}_{-0.80}$	0.103	25.0	31.2	(4, 28, 94)
XTE J1855-026	EB, XP, XT	6.07	1.90E+37	$11.09^{+6.45}_{-3.35}$	$1.80^{0.59}_{-0.58}$	B0Iaep	$19.90^{+1.50}_{-1.40}$	<0.040	22.0	22.9	(4, 28, 41)
4U 1909 + 07	CL, XP	4.40	3.50E+36	$10.71^{+4.29}_{-4.29}$	1.40	O7.5-9.5If	$15.00^{+6.00}_{-6.00}$	0.021	16.0	16.7	(4, 95)
SMC X-1	EB	3.89	⋯	$14.88^{+3.47}_{-2.85}$	$1.21^{+0.12}_{-0.12}$	B0sg	$18.00^{+2.00}_{-2.00}$	0.001	15.0	17.0	(28)
LMC X-4	EB	1.41	3.60E+38	$11.46^{+1.55}_{-1.34}$	$1.57^{+0.11}_{-0.11}$	O8III	$18.00^{+1.00}_{-1.00}$	0.006	7.4	8.4	(28, 96)
					NS-ULXs						
NGC 300 ULX-1	ULX	290.00	5.00E+39	$5.29^{+0.59}_{-0.59}$	$1.70^{+0.30}_{-0.30}$	⋯	9^{+1}_{-1}	⋯	310.0	213.5	(97, 98)
NGC 7793 P13	ULX	64.00	5.00E+39	$14.64^{+1.79}_{-1.79}$	1.40	B9I	$20.50^{+2.50}_{-2.50}$	0.325	⋯	114.4	(99–101)
Swift J0243.6 + 6124	BE, CL, RS, ULX	28.30	2.00E+39	11.43	1.40	O9.5Ve	16.00	0.100	⋯	59.6	(4, 102, 103)
M51 ULX-7	ULX	2.00	1.00E+40	5.93	1.40	⋯	>8.3	0.220	⋯	7.6	(104, 105)
					BHXBs						
MWC 656	BE,BH	60.37	1.00E+32	$2.44^{+0.56}_{-0.56}$	$5.33^{+1.57}_{-1.53}$	B1.5-B2III	$13.00^{+3.00}_{-3.00}$	0.100	10.0	78.1	(106)

Table 1
(Continued)

Name	X-ray Type	$P_{\rm orb}$ (days)	Peak $L_{\rm X}$ (erg s^{-1})	$q = M_{\rm d}/M_{\rm X}$	$M_{\rm X}$ ($M_\odot$)	SpType[a]	$M_{\rm d}$ ($M_\odot$)	e	$R_{\rm d}$ ($R_\odot$)	$R_{\rm L}$ ($R_\odot$)	References
SS 433	BE, BH, EB, MQ, RS	13.10	2.00E+37	$2.69^{+0.14}_{-0.14}$	$4.20^{+0.40}_{-0.40}$	A3-7I	$11.30^{+0.60}_{-0.60}$	⋯	27.2	27.2	(107)
Cyg X-1	BH, MQ, RS, SG, US	5.60	1.40E+37	$1.92^{+0.36}_{-0.33}$	$21.20^{+2.20}_{-2.20}$	O9.7Iabpvar	$40.60^{+7.70}_{-7.10}$	0.019	22.3	22.9	(108)
HD 96670	BE, BH	5.28	2.40E+34	$3.66^{+0.84}_{-0.58}$	$6.20^{+0.90}_{-0.70}$	O8.5f(n)p	$22.70^{+5.20}_{-3.60}$	0.120	17.1	19.3	(109)
LS 5039	BH, GP, RS	3.91	6.00E+34	$6.19^{+0.92}_{-0.78}$	$3.70^{+1.30}_{-1.00}$	ON6V((f))z	$22.90^{+3.40}_{-2.90}$	0.350	9.3	16.8	(2, 110)
SAX J1819.3-2525	BH, XT	2.82	2.88E+39	$0.68^{+0.17}_{-0.11}$	$9.61^{+2.08}_{-0.88}$	B9III	$6.53^{+1.60}_{-1.03}$	⋯	7.5	7.3	(111)
Cyg X-3	BH, MQ, RS	0.20	5.00E+38	$1.61^{+0.17}_{-0.17}$	7.20	WN4-6	$11.60^{+1.20}_{-1.20}$	⋯	8.0	1.6	(112)

Note.
[a] Donor Spectral Type

References: (1) K. H. Hinkle et al. (2020), (2) J. Krtička et al. (2015), (3) R. Hainich et al. (2020), (4) V. Kim et al. (2023), (5) S. Chaty & F. Rahoui (2012), (6) F. Fortin et al. (2020), (7) S. P. Drave et al. (2010), (8) A. Bodaghee et al. (2011), (9) D. T. Koh et al. (1997), (10) L. Kaper et al. (2006), (11) R. Staubert et al. (2019), (12) V. Kim et al. (2023), (13) A. D'Aìet al. (2011), (14) V. La Parola et al. (2010), (15) J. M. Torrejón et al. (2010), (16) C. M. Boon et al. (2016), (17) P. Romano et al. (2010), (18) J. J. M. in't Zand et al. (2007), (19) N. Uchida et al. (2021), (20) C. Ferrigno et al. (2008), (21) L. Prat et al. (2008), (22) L. J. Pellizza et al. (2006), (23) S. P. Drave et al. (2012), (24) E. A. Nikolaeva et al. (2013), (25) I. F. Bikmaev et al. (2017), (26) P. Reig et al. (1996), (27) S. A. Farrell et al. (2008), (28) M. Falanga et al. (2015), (29) M. Ribó et al. (2006), (30) D. Götz et al. (2007), (31) P. Kretschmar et al. (2021), (32) Z. Liao et al. (2020), (33) V. Sguera et al. (2011), (34) N. L. J. Cox et al. (2005), (35) C. Maitra & B. Paul (2013), (36) M. E. Goossens et al. (2013), (37) S. C. Butler et al. (2009), (38) G. Cusumano et al. (2020), (39) P. Romano et al. (2015), (40) S. Chaty et al. (2008), (41) J. B. Coley et al. (2015), (42) G. Cusumano et al. (2016), (43) A. P. Reynolds et al. (1992), (44) P. Reig et al. (1997), (45) J. S. Clark et al. (2001), (46) M. J. Coe et al. (2007), (47) T. Yamamoto et al. (2014), (48) P. Harmanec et al. (2000), (49) J. B. Stevens et al. (1997), (50) K. Belczynski & J. Ziolkowski (2009), (51) Y. Zhao et al. (2023), (52) C. A. Wilson et al. (2003), (53) N. Masetti et al. (2006), (54) C. A. Wilson et al. (1997), (55) J. Yan et al. (2012), (56) P. Reig et al. (2001), (57) C. Motch et al. (1997), (58) G. Cusumano et al. (2013), (59) N. D. Richardson et al. (2023), (60) P. Reig et al. (2023), (61) T. Bouchet et al. (2022), (62) M. T. Stollberg et al. (1999), (63) C. Malacaria et al. (2023), (64) M. H. Finger et al. (1996), (65) I. Negueruela et al. (2003), (66) D. K. Galloway et al. (2004), (67) H. Raichur & B. Paul (2010), (68) J. Casares et al. (2005a), (69) I. Negueruela & A. T. Okazaki (2001), (70) S. Müller et al. (2013), (71) D. K. Galloway et al. (2005), (72) K. Koyama et al. (1991), (73) E. A. Barsukova et al. (2006), (74) E. S. Bartlett et al. (2019), (75) P. G. Jonker et al. (2007), (76) N. S. Schulz et al. (2020), (77) R. H. D. Corbet et al. (2019), (78) E. A. Saavedra et al. (2023), (79) A. Baykal et al. (2000), (80) P. Reig et al. (2004), (81) P. Kaaret et al. (2000), (82) M. J. Coe & J. A. Orosz (2000), (83) A. Sierpowska-Bartosik & W. Bednarek (2008), (84) I. Negueruela et al. (2011), (85) J. Casares et al. (2012), (86) Y. Moritani et al. (2018), (87) M. H. Finger et al. (1999), (88) A. Nabizadeh et al. (2022), (89) J. J. M. in't Zand et al. (2001), (90) R. H. D. Corbet et al. (2009), (91) M. Bissinger (2016), (92) A. Salganik et al. (2022), (93) B. van Soelen et al. (2022), (94) A. B. Mason et al. (2009), (95) S. Martínez-Núñez et al. (2015), (96) R. Sharma et al. (2023), (97) M. Heida et al. (2019), (98) A. King et al. (2023), (99) C. Motch et al. (2011), (100) C. Motch et al. (2014), (101) D. Misra et al. (2020), (102) V. Doroshenko et al. (2018), (103) P. Reig et al. (2020), (104) G. A. Rodríguez Castillo et al. (2020), (105) A. King et al. (2023), (106) J. Casares et al. (2014), (107) P. Picchi et al. (2020), (108) J. C. A. Miller-Jones et al. (2021), (109) S. Gomez & J. E. Grindlay (2021), (110) J. Casares et al. (2005b), (111) J. A. Orosz et al. (2001), (112) I. I. Antokhin et al. (2022).

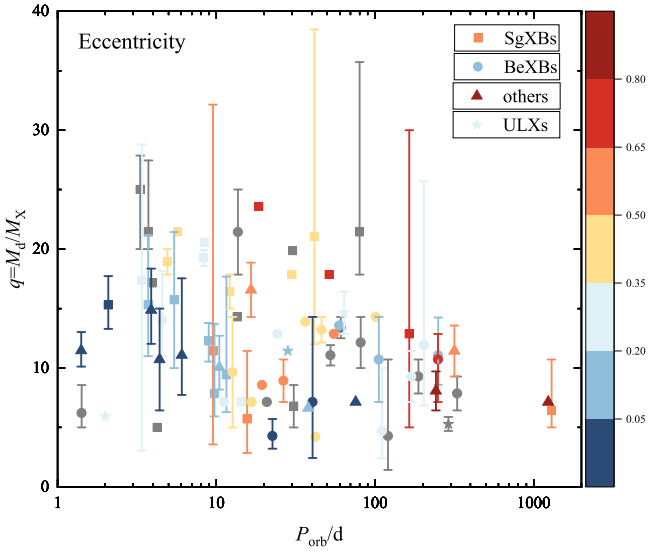

Figure 9. The eccentricities of HMXBs on a mass-ratio against the orbital-period diagram. The symbols again show the HMXB types.

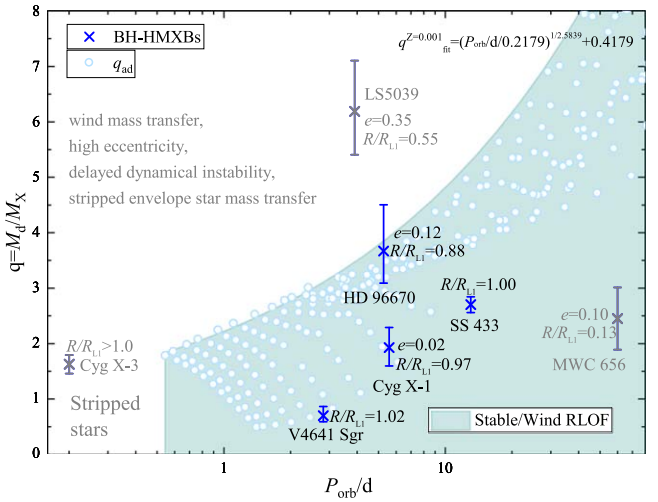

Figure 10. Seven BH-HMXBs in a mass-ratio against the orbital-period diagram. Blue symbols mark objects with a high overfilling factor R/R_L and low eccentricity e. Gray symbols show wind mass-transferring objects or HMXBs with a near naked helium star donor. Blue open circles, with white dots inside that scattered in the colored area, are the critical mass ratios for the dynamical-timescale mass transfer of massive stars in different evolutionary states. The upper boundary of the blue region is a fit of the critical mass ratio as a function of the orbital period.

Only seven HMXBs composed with a BH accretor have known binary parameters (Table 1). We plot these BH-HMXBs in a mass-ratio against the orbital-period diagram (Figure 10). Four have a low eccentricity and high overfilling factor (blue) and are suitable sources to compare with the theoretical mass-ratio limits. MWC 656 and LS 5039 (gray) are wind-driven HMXBs. Cyg X-3 contains a WN 4 to 6 type donor star, which is significantly smaller than a massive MS star. The blue open circles mark the critical mass ratio for massive metal-poor ($Z=0.001$) donor stars in different evolutionary states. We fit the maximum critical mass ratio q_{ad} envelope as a function of the orbital period. We only show the fitting of $Z=0.001$ massive stars for simplicity. The maximum critical mass ratios q_{ad}^{max} of $Z=0.02$ massive stars are slightly larger than $Z=0.001$ donors. These observed BH-HMXBs in circular orbits and transferring mass through RLOF are located below our theoretically predicated mass-ratio limits, as required.

Any systems above the blue envelope must be in a wind mass transfer phase or possibly undergoing thermal RLOF before experiencing a delayed dynamical instability. Indeed, LS 5039 has a high eccentricity that is less correlated with RLOF.

Similarly, we select 14 HMXB systems with NS companions and eccentricity $e<0.35$. We plot these NS-HMXBs in a mass-ratio against orbital-period diagram (Figure 11). Eight (violet) NS-HMXBs have known donor radii. The other six (gray) do not. We color the stable mass transfer parameter space for low-metallicity ($Z=0.001$) hydrogen-rich donor stars blue in Figure 11, similarly to Figure 10. So, binary systems above the blue envelope are only possible for wind mass transfer and thermal timescale mass transfer before entering delayed dynamically unstable mass transfer, or if the donor is a naked helium star. Our predicted mass-ratio upper limits are for stable mass transfer in a circular orbit. With relatively long orbital periods ($P_{orb}>11$ days) NS-HMXBs, two eccentric systems are located above the critical mass-ratio limit. These are most likely in a wind mass transfer phase. With relatively short orbital periods ($P_{orb}<11$ days), all eight systems are located above the critical mass-ratio limit. Seven have R/R_L larger than 0.96 and so must be in a state of relatively stable RLOF. They may almost be ready to experience a delayed dynamical instability. However, this stage is expected to last only for a short thermal timescale. A more likely explanation is that their donors are helium stars[10]. We extrapolate the results of L. Zhang et al. (2024) and fit the maximum critical mass ratios of solar-metallicity helium donor stars. We find these short-period NS-HMXBs are then under the critical mass-ratio limit, except for one ready constrained eccentric system. We encourage more detailed observations to test this hypothesis.

6. Discussions

We have considered the impact of both metallicity and nonconservative mass transfer on the dynamical-timescale mass transfer thresholds. Similarly to our previous study (H. Ge et al. 2023), metal-poor stars on the MS or HG (radiative envelope) tend to be more unstable than metal-rich donors (Figure 4). Metal-poor donors, with deep convective envelopes, are more stable than metal-rich stars (Figure 4). We expect that mass transfer stability thresholds may impact binary systems differently in the Galactic thick and thin disks and the halo.

Nonconservative mass transfer significantly decreases the critical mass ratio for massive donors that have left the MS compared with the conservative case (Figure 7). Nevertheless, the critical mass ratios of massive MS and HG donors are mostly still greater than 3 or 4. This suggests a moderate increase in the number of binary systems that form from stable mass transfer channels.

Stellar winds may significantly change the masses of the donor and the orbital separation before Roche-lobe filling. Such winds are included in binary population synthesis studies. Our initial donor stars that fill their Roche lobes are built without

[10] Helium stars in such short orbital periods can be formed through a previous binary interaction process, e.g., common envelope ejection. The current helium donor star either is reaching its thermal equilibrium right after the common envelope evolution or nearly overfills its Roche lobe due to evolution expansion.

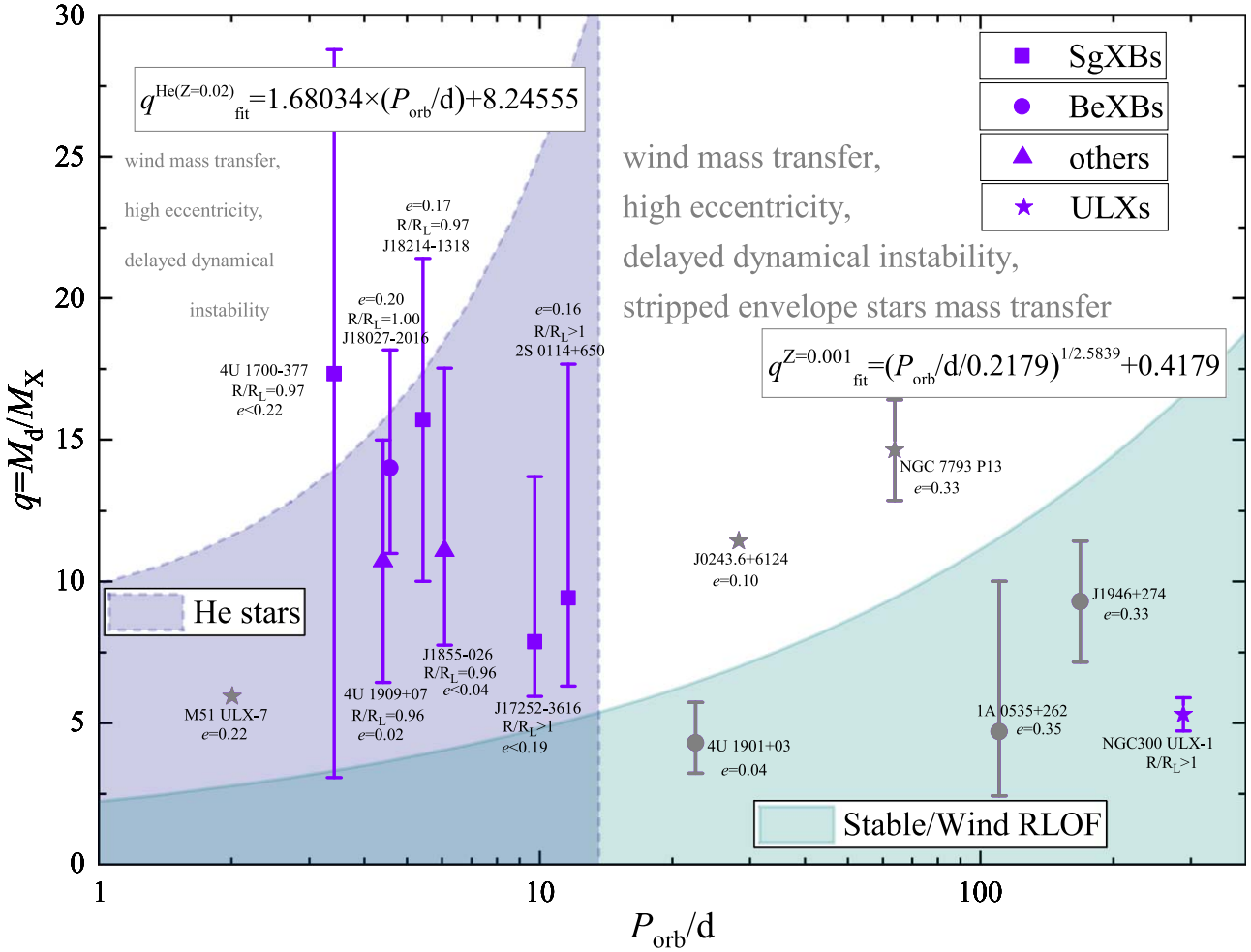

Figure 11. Fourteen NS-HMXBs on a mass-ratio against orbital-period diagram. Symbols mark different types of NS-HMXBs. Violet NS-HMXBs have measured radii, while gray do not. The blue and violet regions are theoretically permitted spaces for stable RLOF from the normal and naked helium donors. Above the fitted maximum mass-ratio envelope (blue for metal-poor $Z = 0.001$ massive donors and violet for $Z = 0.02$ helium donor stars), systems must be undergoing wind mass transfer, have a highly eccentric orbit, and be suffering delayed dynamical instability.

wind mass loss (H. Ge et al. 2010) in order to minimize the impact of the uncertainty of stellar winds. Both observation (M. R. Mokiem et al. 2007) and theory (P. S. Conti et al. 2008) suggest that stellar wind is metallicity-sensitive. We previously considered the impact of stellar wind (H. Ge et al. 2020a) and found that the critical mass ratio of a donor depends on the initial mass of the donor and its current core mass, both of which are evaluated in population synthesis models (J. R. Hurley et al. 2002) in a different way.

Rotation is also important in massive star evolution. Rotation and extra mixing (G. Meynet & A. Maeder 2003, 2005) can enhance the formation of Wolf–Rayet stars. Indeed, S. J. Smartt et al. (2004) noticed and P. Massey et al. (2017) reported a lack of RSGs in Local Group galaxies. So rotation and extra mixing are worthy of future work in mass transfer physics.

Our systematic studies of the thresholds for dynamical-timescale mass transfer predict the onset of the CE evolution (B. Paczynski 1976). After the critical mass ratios for unstable mass transfer, the treatment of CE ejection is the next least understood question in binary star evolution. The current treatment requires both precise binding energy $E_{\rm bind}$ (Z. Chen & N. Ivanova 2024) and CE ejection efficiency $\alpha_{\rm CE}$ (P. Scherbak & J. Fuller 2023; H. Ge et al. 2024). H. Ge et al. (2022, 2024) found evidence for a relation between the initial mass ratio and their common envelope ejection efficiency $\beta_{\rm CE}$ for low-mass ($M_{\rm i} < 2\,M_{\odot}$) donor stars. So, this work should also be extended to higher mass stars.

7. Summary

Previously, H. Ge et al. (2010, 2015, 2020a) systematically presented critical mass ratios, assumed conserved mass and angular momentum, for dynamical-timescale mass transfer over the entire span of donor star evolutionary states with $Z = 0.02$. Here, we extend our analysis to include various metallicities and nonconservative mass transfer. Using 20 $M_{\odot}$ donor stars as examples, we analyze the response of stars with metallicities $Z = 0.02$ and $Z = 0.001$ with nonconservative mass transfer. We find the critical mass ratios of donor stars with masses between 1 and 100 $M_{\odot}$ with $Z = 0.001$. We further complement the thresholds for nonconservative unstable mass transfer for stars between 0.1 and 100 $M_{\odot}$ at $Z = 0.02$. Critical mass ratios of metal-poor MS and HG donors with radiative envelopes are smaller than those of solar-metallicity stars at the same evolutionary stage. However, critical mass ratios of metal-poor RGB/AGB donors with a convective envelope are larger than those of the solar metallicity with the same radii. Nonconservative mass transfer also decreases the critical mass ratios of donors from late-MS to the end of the star's evolution. We

apply our results to 82 observed HMXBs with measured mass ratios and orbital periods. The observed HMXBs with low eccentricities and overfilled Roche lobes are nicely located under our predicted limits. Our results can be applied to study individual binary objects and binary population synthesis of most binary systems.

Acknowledgments

We thank the referee for the valuable comments and suggestions. This project is supported by the National Natural Science Foundation of China (NSFC Nos. 12288102, 12125303, 12090040/3, 12173081, 12273057, 12473034, 12103086, 12233002, U2031205), the National Key R&D Program of China (Nos. 2021YFA1600403, 2021 YFA1600401, 2021YFA0718500), the Key Research Program of Frontier Sciences, CAS (No. ZDBS-LY-7005), CAS-Light of West China Program, Yunnan Fundamental Research Projects (Nos. 202101AV070001, 202201BC070003, 202401 BC070007, 202401AT070139, 202201AU070234), Yunnan Revitalization Talent Support Program—Science & Technology Champion Project (No. 202305AB350003), and the International Centre of Supernovae, Yunnan Key Laboratory (No. 202302AN360001). H.G. thanks Professor Ronald Webbink for helpful discussions in building the adiabatic mass-loss model. H.G. thanks Boyuan Liu, a postdoctoral research associate at the Institute of Astronomy at the University of Cambridge, for useful comments. C.A.T. thanks Churchill College for the fellowship.

Appendix
Tables for the Initial Physical Properties of Donor Stars and the Thresholds for Dynamical-timescale Mass Transfer

We present the interior physical properties of metal-poor stars in Table A1. Only model sequences for 20 $M_\odot$ donors are listed in this printed table. Further models are available in machine-readable form. The physical parameters are:

1. n—mass-loss sequence number counting from ZAMS,
2. $M_{\rm i}$—initial mass of the mass-transferring star ($M_\odot$),
3. $\log_{10} t$—age (yr),
4. $M_{\rm He}$—helium core mass ($M_\odot$), where the hydrogen abundance X first reaches 0.15 going out from the center,
5. $M_{\rm C}$—carbon core mass ($M_\odot$), where the helium abundance Y first reaches 0.25,
6. $M_{\rm deg}$—mass of the degenerate core ($M_\odot$),
7. $M_{\rm ce}$—mass of the convective envelope ($M_\odot$),
8. $\psi_{\rm c}$—central electron chemical potential ($\mu_{\rm e}$, in units of kT),
9. $\log_{10}\rho_{\rm c}$—central density (g cm^{-3}),

Table A1
Interior Physical Properties of Metal-poor Donor Stars

n	$M_{\rm i}$ ($M_\odot$)	$\log_{10} t$ (yr)	$M_{\rm He}$ ($M_\odot$)	$M_{\rm C}$ ($M_\odot$)	$M_{\rm deg}$[a] ($M_\odot$)	$M_{\rm ce}$ ($M_\odot$)	$\psi_{\rm c}$ kT	$\log_{10}\rho_{\rm c}$ (g cm^{-3})	$\log_{10} T_{\rm c}$ (K)	$X_{\rm c}$	$Y_{\rm c}$	$X_{\rm s}$
1	20.00	4.29823[b]	0.0000	0.0000	0.0000	0.0000	−5.813	0.847	7.602	0.755	0.244	0.756
2	20.00	6.11811	0.0000	0.0000	0.0000	0.0000	−5.867	0.844	7.606	0.702	0.297	0.756
3	20.00	6.53654	0.0000	0.0000	0.0000	0.0000	−5.964	0.845	7.617	0.597	0.402	0.756
4	20.00	6.69735	0.0000	0.0000	0.0000	0.0000	−6.047	0.851	7.627	0.502	0.497	0.756
5	20.00	6.80333	0.0000	0.0000	0.0000	0.0000	−6.129	0.863	7.639	0.400	0.599	0.756
6	20.00	6.86733	0.0000	0.0000	0.0000	0.0000	−6.195	0.882	7.651	0.308	0.691	0.756
7	20.00	6.91894	0.0000	0.0000	0.0000	0.0000	−6.254	0.918	7.668	0.204	0.795	0.756
8	20.00	6.95590	6.4784	0.0000	0.0000	0.0000	−6.279	0.984	7.693	0.100	0.899	0.756
9	20.00	6.97635	6.4439	0.0000	0.0000	0.0000	−6.203	1.116	7.738	0.023	0.976	0.756
10	20.00	6.98154	6.4464	0.0000	0.0000	0.0000	−5.404	1.758	7.926	0.000	0.999	0.756
11	20.00	6.98180	6.0535	0.0000	0.0000	0.0000	−4.663	2.231	8.025	0.000	0.999	0.756
12	20.00	6.98194	5.9880	0.0000	0.0000	0.0000	−4.293	2.493	8.091	0.000	0.999	0.756
13	20.00	6.98207	5.9508	0.0000	0.0000	0.0000	−3.998	2.716	8.153	0.000	0.999	0.756
14	20.00	6.98219	5.9264	0.0000	0.0000	0.0000	−3.810	2.889	8.213	0.000	0.998	0.756
15	20.00	6.98230	5.9143	0.0000	0.0000	0.0000	−3.803	2.933	8.239	0.000	0.995	0.756
16	20.00	6.98243	5.9102	0.0000	0.0000	0.0000	−3.841	2.922	8.243	0.000	0.991	0.756
17	20.00	6.98260	5.9129	0.0000	0.0000	0.0000	−3.868	2.911	8.243	0.000	0.986	0.756
18	20.00	6.98305	5.9355	0.0000	0.0000	0.0000	−3.887	2.905	8.244	0.000	0.972	0.756
19	20.00	6.98667	6.2021	0.0000	0.0000	0.0000	−3.939	2.896	8.253	0.000	0.859	0.756
20	20.00	6.99093	6.5194	0.0000	0.0000	0.0000	−3.986	2.893	8.264	0.000	0.730	0.756
21	20.00	6.99534	6.8261	0.0000	0.0000	0.0000	−4.024	2.896	8.277	0.000	0.598	0.756
22	20.00	6.99987	7.1116	0.0000	0.0000	0.0000	−4.048	2.908	8.291	0.000	0.467	0.756
23	20.00	7.00351	7.3153	0.0000	0.0000	0.0000	−4.055	2.924	8.304	0.000	0.366	0.756
24	20.00	7.00612	7.4467	0.0000	0.0000	0.0000	−4.053	2.942	8.314	0.000	0.296	0.756
25	20.00	7.00787	7.5275	0.0000	0.0000	0.0002	−4.047	2.957	8.322	0.000	0.252	0.756
26	20.00	7.00895	7.5746	5.1621	0.0000	0.0115	−4.042	2.967	8.327	0.000	0.225	0.756
27	20.00	7.00952	7.5989	5.2912	0.0000	0.0322	−4.038	2.973	8.330	0.000	0.212	0.756
28	20.00	7.00990	7.6143	5.3466	0.0000	0.2851	−4.036	2.977	8.332	0.000	0.204	0.756
29	20.00	7.01166	7.6771	5.5674	0.0000	5.4279	−4.020	2.999	8.342	0.000	0.164	0.756
30	20.00	7.02019	7.9333	5.8987	0.0000	9.8211	−3.204	3.736	8.585	0.000	0.000	0.741

Notes.
[a] The degenerate core mass only makes sense for low- and intermediate-mass stars but not for massive stars.
[b] The age of the ZAMS star is not zero because it contracts slightly to reach a minimum radius after core hydrogen burning.

(This table is available in its entirety in machine-readable form in the online article.)

Table A2
Global Physical Properties of Metal-poor Donor Stars

n	M_i ($M_\odot$)	$\log_{10}R_i$ ($R_\odot$)	$\log_{10}T_{eff}$ (K)	$\log_{10}L$ ($L_\odot$)	$\log_{10}t_{KH}$ (yr)	$k^2=I/(M_iR_i^2)$	L_H ($L_\odot$)	L_{He} ($L_\odot$)	L_Z ($L_\odot$)	$\lvert L_{neu}\rvert$ ($L_\odot$)	L_{th} ($L_\odot$)
1	20.00	0.6619	4.5864	4.6227	4.8126	9.5611E-02	4.4605E+04	7.2782E-19	0.0000E+00	2.8758E+03	2.1898E+02
2	20.00	0.6829	4.5853	4.6604	4.7538	9.0493E-02	4.8692E+04	1.2382E-18	0.0000E+00	3.1314E+03	1.9047E+02
3	20.00	0.7264	4.5814	4.7317	4.6391	8.0609E-02	5.7370E+04	3.5298E-18	0.0000E+00	3.6785E+03	2.1697E+02
4	20.00	0.7703	4.5745	4.7921	4.5347	7.2018E-02	6.5934E+04	8.8420E-18	0.0000E+00	4.2192E+03	2.3954E+02
5	20.00	0.8246	4.5629	4.8540	4.4185	6.3049E-02	7.6044E+04	2.4612E-17	0.0000E+00	4.8586E+03	2.6624E+02
6	20.00	0.8804	4.5480	4.9062	4.3106	5.5405E-02	8.5746E+04	6.6279E-17	0.0000E+00	5.4733E+03	2.9407E+02
7	20.00	0.9533	4.5253	4.9608	4.1831	4.7336E-02	9.7253E+04	2.4640E-16	0.0000E+00	6.2035E+03	3.1832E+02
8	20.00	1.0364	4.4960	5.0102	4.0506	4.0028E-02	1.0897E+05	1.5946E-15	0.0000E+00	6.9483E+03	3.4505E+02
9	20.00	1.0886	4.4785	5.0443	3.9642	3.5284E-02	1.1759E+05	4.0070E-14	0.0000E+00	7.4971E+03	6.4378E+02
10	20.00	1.0230	4.5216	5.0858	3.9884	3.1714E-02	9.7016E+04	2.0580E-08	0.0000E+00	6.1882E+03	3.1005E+04
11	20.00	1.1214	4.4726	5.0864	3.8893	2.9389E-02	1.2727E+05	4.3474E-04	0.0000E+00	8.1177E+03	2.8640E+03
12	20.00	1.2227	4.4273	5.1078	3.7666	2.5969E-02	1.3177E+05	3.6568E-01	1.8090E-39	8.4045E+03	4.8165E+03
13	20.00	1.3212	4.3817	5.1225	3.6535	2.3269E-02	1.3212E+05	9.3762E+01	5.1829E-35	8.4266E+03	8.8000E+03
14	20.00	1.4203	4.3348	5.1332	3.5436	2.0915E-02	1.2911E+05	8.2745E+03	3.1811E-29	8.2368E+03	6.7365E+03
15	20.00	1.5191	4.2881	5.1437	3.4344	1.8612E-02	1.1810E+05	4.0547E+04	1.4221E-26	7.5366E+03	-1.1900E+04
16	20.00	1.6227	4.2400	5.1586	3.3158	1.6018E-02	1.1558E+05	4.7246E+04	9.6270E-26	7.3765E+03	-1.1380E+04
17	20.00	1.7289	4.1910	5.1749	3.1934	1.3439E-02	1.1701E+05	4.5724E+04	2.9139E-25	7.4677E+03	-5.6908E+03
18	20.00	1.8236	4.1471	5.1889	3.0846	1.1311E-02	1.1681E+05	4.5809E+04	1.4271E-24	7.4553E+03	-6.6743E+02
19	20.00	1.9235	4.1002	5.2009	2.9727	9.3513E-03	1.1231E+05	5.3882E+04	1.0912E-22	7.1697E+03	-1.9171E+02
20	20.00	2.0233	4.0529	5.2114	2.8625	7.6560E-03	1.0532E+05	6.4253E+04	1.3817E-21	6.7283E+03	-1.5158E+02
21	20.00	2.1219	4.0059	5.2207	2.7546	6.2239E-03	9.6559E+04	7.5929E+04	1.1673E-20	6.1754E+03	-1.0413E+02
22	20.00	2.2232	3.9573	5.2287	2.6453	5.0165E-03	8.6217E+04	8.8652E+04	9.1919E-20	5.5251E+03	-3.5717E+01
23	20.00	2.3241	3.9082	5.2341	2.5389	4.1074E-03	7.7279E+04	9.9131E+04	4.8220E-19	4.9660E+03	-2.8225E+00
24	20.00	2.4243	3.8589	5.2375	2.4354	3.5368E-03	7.0453E+04	1.0674E+05	1.6826E-18	4.5415E+03	1.1836E+02
25	20.00	2.5217	3.8107	5.2392	2.3363	3.2843E-03	6.5806E+04	1.1182E+05	4.0214E-18	4.2545E+03	9.2922E+01
26	20.00	2.6240	3.7595	5.2395	2.2336	3.3526E-03	6.2869E+04	1.1493E+05	6.9895E-18	4.0740E+03	-1.5093E+02
27	20.00	2.7242	3.7091	5.2381	2.1349	4.1434E-03	6.1136E+04	1.1658E+05	9.3677E-18	3.9674E+03	-7.3906E+02
28	20.00	2.8234	3.6566	5.2266	2.0471	1.2175E-02	5.8794E+04	1.1761E+05	1.1330E-17	3.8208E+03	-4.0798E+03
29	20.00	2.8730	3.6329	5.2309	1.9933	5.2887E-02	5.0393E+04	1.2256E+05	3.0375E-17	3.3009E+03	5.1427E+02
30	20.00	2.9294	3.6221	5.3003	1.8673	8.8615E-02	5.7779E+04	3.6313E+04	1.2399E-07	8.3165E+03	1.1390E+05

(This table is available in its entirety in machine-readable form in the online article.)

10. $\log_{10}T_c$—central temperature (K),
11. X_c—central hydrogen mass fraction,
12. Y_c—central helium mass fraction, and
13. X_s—surface hydrogen mass fraction.

Second, we document the global physical properties of metal-poor stars in Table A2. As for Table A1, only model sequences of $20\,M_\odot$ donors are listed in this printed table. Again, the full data are available online in machine-readable form. The variables are listed as follows:

1. n—mass-loss sequence number,
2. M_i—initial mass of the mass-transferring star ($M_\odot$),
3. $\log_{10}R_i$—initial radius of the donor star ($R_\odot$),
4. $\log_{10}T_{eff}$—effective temperature (K),
5. $\log_{10}L$—stellar luminosity ($L_\odot$),
6. $\log_{10}t_{KH}$—thermal, Kelvin–Helmholtz, timescale (yr),
7. $k^2=I/(M_iR_i^2)$—dimensionless moment of inertia,
8. L_H—hydrogen-burning luminosity ($L_\odot$),
9. L_{He}—helium-burning luminosity ($L_\odot$),
10. L_Z—heavy-element (carbon-, oxygen- etc.) burning luminosity ($L_\odot$),
11. $|L_{neu}|$—neutrino luminosity ($L_\odot$), and
12. L_{th}—gravothermal luminosity ($L_\odot$).

Third, we summarize the quantitative results of thresholds for both conservative and nonconservative dynamical-timescale mass transfer in Table A3. The superscripts in Table A3 indicate $\beta\in\{1,\ 0.5,\ 0\}$. During the mass transfer process, a fraction $(1-\beta)$ of mass is lost from the system and takes away the specific angular momentum of the accretor. Columns (4)–(10) list the dynamical mass transfer thresholds for standard stellar models, and columns (11)–(17) are for models with artificially isentropic convective envelopes (a ∼on a variable top). The variables are:

1. n—mass-loss sequence number,
2. M_i—initial mass of the mass-transferring star ($M_\odot$),
3. $\log_{10}R_i$—initial radius of the donor star ($R_\odot$),
4. ζ_{ad}^1—critical radius-mass exponent for conservative dynamical-timescale mass transfer,
5. q_{ad}^1—critical initial mass ratio for conservative dynamical-timescale mass transfer,
6. M_{KH}^1—mass threshold at which $\dot{M}=-M_i/t_{KH}$ and the tangent point for the minimum q_{ad}^1,
7. $q_{ad}^{0.5}$—critical initial mass ratio for semiconservative dynamical-timescale mass transfer,
8. $M_{KH}^{0.5}$—mass threshold at which $\dot{M}=-M_i/t_{KH}$ and the tangent point for the minimum $q_{ad}^{0.5}$,
9. q_{ad}^0—critical initial mass ratio for fully nonconservative dynamical-timescale mass transfer,
10. M_{KH}^0—mass threshold at which $\dot{M}=-M_i/t_{KH}$ and the tangent point for the minimum q_{ad}^0,

Table A3
Thresholds for Conservative to Nonconservative Dynamical-timescale Mass Transfer of $Z = 0.001$ Donor Stars

n	M_i ($M_\odot$)	$\log_{10}R_i$ ($R_\odot$)	ζ_{ad}^{1}	q_{ad}^{1}	M_{KH}^{1} ($M_\odot$)	$q_{ad}^{0.5}$	$M_{KH}^{0.5}$ ($M_\odot$)	q_{ad}^{0}	M_{KH}^{0} ($M_\odot$)	$\tilde{\zeta}_{ad}^{1}$	$\tilde{q}_{ad}^{1}$	$\tilde{M}_{KH}^{1}$ ($M_\odot$)	$\tilde{q}_{ad}^{0.5}$	$\tilde{M}_{KH}^{0.5}$ ($M_\odot$)	$\tilde{q}_{ad}^{0}$	$\tilde{M}_{KH}^{0}$ ($M_\odot$)
1	20.00	0.6619	1.576	1.520	12.572	1.638	12.082	1.687	10.903	1.576	1.519	12.579	1.638	12.067	1.687	10.923
2	20.00	0.6829	1.702	1.578	12.723	1.693	12.224	1.738	11.115	1.702	1.578	12.723	1.693	12.224	1.738	11.115
3	20.00	0.7264	1.969	1.703	12.952	1.808	12.485	1.835	11.520	1.969	1.703	12.952	1.808	12.485	1.835	11.520
4	20.00	0.7703	2.235	1.826	13.128	1.921	12.667	1.929	11.746	2.233	1.826	13.122	1.921	12.660	1.929	11.756
5	20.00	0.8246	2.557	1.976	13.330	2.057	12.851	2.042	11.925	2.557	1.977	13.345	2.056	12.840	2.041	11.864
6	20.00	0.8804	2.886	2.130	13.531	2.194	13.054	2.152	12.024	2.886	2.130	13.532	2.194	13.048	2.152	12.010
7	20.00	0.9533	3.308	2.327	13.716	2.368	13.239	2.291	12.172	3.308	2.327	13.716	2.368	13.239	2.291	12.172
8	20.00	1.0364	3.787	2.551	13.924	2.562	13.408	2.442	12.277	3.788	2.552	13.924	2.562	13.408	2.442	12.277
9	20.00	1.0886	4.172	2.732	14.051	2.716	13.562	2.560	12.392	4.172	2.731	14.072	2.715	13.557	2.560	12.396
10	20.00	1.0230	4.479	2.876	14.300	2.842	13.764	2.663	12.689	4.479	2.876	14.300	2.842	13.764	2.663	12.689
11	20.00	1.1214	4.552	2.910	14.343	2.873	13.870	2.692	12.870	4.553	2.910	14.342	2.874	13.869	2.693	12.869
12	20.00	1.2227	5.022	3.130	14.380	3.053	13.876	2.818	12.779	5.028	3.133	14.379	3.055	13.874	2.819	12.776
13	20.00	1.3212	5.481	3.346	14.389	3.224	13.855	2.933	12.684	5.492	3.351	14.385	3.228	13.851	2.935	12.678
14	20.00	1.4203	5.965	3.573	14.379	3.402	13.815	3.048	12.571	5.983	3.582	14.373	3.408	13.808	3.052	12.562
15	20.00	1.5191	6.536	3.842	14.407	3.609	13.804	3.183	12.498	6.562	3.854	14.400	3.618	13.795	3.188	12.485
16	20.00	1.6227	7.335	4.218	14.476	3.895	13.850	3.368	12.454	7.376	4.238	14.466	3.909	13.839	3.375	12.438
17	20.00	1.7289	8.344	4.694	14.548	4.248	13.887	3.587	12.406	8.408	4.725	14.536	4.269	13.872	3.598	12.383
18	20.00	1.8236	9.408	5.197	14.611	4.609	13.918	3.803	12.360	9.502	5.242	14.594	4.638	13.899	3.818	12.332
19	20.00	1.9235	10.622	5.772	14.670	5.009	13.938	4.034	12.351	10.757	5.836	14.651	5.050	13.916	4.054	12.319
20	20.00	2.0233	12.014	6.432	14.725	5.455	13.955	4.280	12.340	12.206	6.523	14.702	5.511	13.929	4.306	12.302
21	20.00	2.1219	13.616	7.193	14.790	5.950	13.967	4.541	12.311	13.885	7.321	14.759	6.026	13.937	4.574	12.258
22	20.00	2.2232	15.506	8.092	14.845	6.514	13.973	4.821	12.257	15.882	8.271	14.815	6.616	13.939	4.863	12.204
23	20.00	2.3241	17.579	9.080	14.873	7.108	13.969	5.097	12.184	18.108	9.333	14.840	7.246	13.924	5.150	12.122
24	20.00	2.4243	19.752	10.118	14.924	7.708	13.986	5.361	12.105	20.875	10.655	14.858	7.989	13.915	5.463	12.001
25	20.00	2.5217	22.012	11.199	14.948	8.311	13.987	5.613	12.020	24.449	12.366	14.848	8.895	13.864	5.812	11.805
26	20.00	2.6240	24.641	12.458	14.791	8.985	14.005	5.878	11.911	29.519	14.800	14.803	10.093	13.790	6.225	11.574
27	20.00	2.7242	27.470	13.816	14.924	9.678	14.024	6.139	11.749	37.011	18.407	14.746	11.719	13.718	6.719	11.236
28	20.00	2.8234	29.117	14.607	14.946	10.100	14.193	6.362	11.866	46.343	22.914	14.724	13.622	13.819	7.282	10.962
29	20.00	2.8730	13.015	6.907	16.106	6.048	15.763	5.044	15.176	23.739	12.026	15.673	9.102	15.246	6.484	14.278
30	20.00	2.9294	10.891	5.900	14.318	5.058	13.672	4.041	12.411	18.087	9.323	13.728	7.013	12.942	4.887	11.655

(This table is available in its entirety in machine-readable form in the online article.)

Table A4
Thresholds for Conservative to Nonconservative Dynamical-timescale Mass Transfer of $Z = 0.02$ Donor Stars

n	M_i ($M_\odot$)	$\log_{10}R_i$ ($R_\odot$)	ζ_{ad}^{1}	q_{ad}^{1}	M_{KH}^{1} ($M_\odot$)	$q_{ad}^{0.5}$	$M_{KH}^{0.5}$ ($M_\odot$)	q_{ad}^{0}	M_{KH}^{0} ($M_\odot$)	$\tilde{\zeta}_{ad}^{1}$	$\tilde{q}_{ad}^{1}$	$\tilde{M}_{KH}^{1}$ ($M_\odot$)	$\tilde{q}_{ad}^{0.5}$	$\tilde{M}_{KH}^{0.5}$ ($M_\odot$)	$\tilde{q}_{ad}^{0}$	$\tilde{M}_{KH}^{0}$ ($M_\odot$)
1	20.00	0.7790	1.896	1.669	12.015	1.765	11.483	1.777	10.291	1.904	1.672	12.004	1.769	11.472	1.779	10.278
2	20.00	0.8239	2.198	1.809	12.264	1.893	11.847	1.885	10.553	2.211	1.815	12.248	1.898	11.833	1.890	10.029
3	20.00	0.8777	2.563	1.980	12.510	2.044	12.021	2.007	10.717	2.586	1.990	12.491	2.053	12.004	2.013	10.665
4	20.00	0.9360	2.972	2.170	12.701	2.210	12.222	2.135	10.763	3.008	2.187	12.675	2.224	12.198	2.144	10.679
5	20.00	1.0066	3.484	2.410	12.907	2.416	12.403	2.287	10.751	3.543	2.437	12.874	2.438	12.366	2.300	10.646
6	20.00	1.0940	4.151	2.722	13.110	2.676	12.570	2.471	10.708	4.244	2.765	13.070	2.710	12.514	2.490	10.589
7	20.00	1.1909	4.943	3.093	13.266	2.976	12.705	2.676	10.664	5.084	3.159	13.220	3.025	12.633	2.702	10.520
8	20.00	1.2612	5.682	3.440	13.402	3.248	12.799	2.859	10.776	5.876	3.531	13.348	3.314	12.721	2.893	10.623
9	20.00	1.1983	5.946	3.565	13.635	3.353	13.088	2.958	11.503	6.189	3.679	13.577	3.436	13.004	3.003	11.340
10	20.00	1.2973	6.268	3.716	13.671	3.469	13.122	3.040	11.801	6.524	3.836	13.608	3.555	13.048	3.088	11.676
11	20.00	1.3991	7.106	4.110	13.641	3.758	13.047	3.212	11.620	7.399	4.249	13.580	3.854	12.968	3.266	11.377
12	20.00	1.5013	8.001	4.532	13.647	4.057	12.951	3.380	11.431	8.332	4.689	13.566	4.161	12.885	3.433	11.293
13	20.00	1.6029	8.939	4.976	13.690	4.365	12.911	3.546	11.247	9.306	5.149	13.617	4.476	12.824	3.599	11.089
14	20.00	1.7035	9.923	5.441	13.765	4.682	12.915	3.711	11.034	10.326	5.632	13.705	4.801	12.836	3.765	10.924
15	20.00	1.8074	10.996	5.949	13.864	5.023	12.956	3.884	10.845	11.445	6.162	13.809	5.152	12.877	3.939	10.730
16	20.00	1.9068	12.090	6.468	13.990	5.366	13.011	4.057	10.681	12.594	6.707	13.929	5.506	12.934	4.113	10.568
17	20.00	2.0087	13.301	7.043	14.114	5.738	13.099	4.240	10.556	13.918	7.337	14.048	5.906	13.005	4.304	10.429
18	20.00	2.1065	14.586	7.654	14.236	6.125	13.168	4.424	10.462	15.306	7.997	14.168	6.316	13.074	4.494	10.311
19	20.00	2.2163	16.197	8.421	14.377	6.597	13.249	4.641	10.350	17.052	8.829	14.306	6.817	13.161	4.717	10.181
20	20.00	2.3061	17.590	9.086	14.494	6.998	13.319	4.820	10.272	18.747	9.638	14.409	7.287	13.214	4.915	10.072
21	20.00	2.4227	19.332	9.917	14.668	7.499	13.454	5.047	10.258	21.398	10.905	14.537	7.999	13.280	5.200	9.924
22	20.00	2.5158	20.777	10.608	14.706	7.907	13.585	5.232	10.258	24.051	12.176	14.573	8.681	13.331	5.456	9.759
23	20.00	2.6188	22.409	11.389	14.473	8.334	13.745	5.435	10.298	27.870	14.008	14.495	9.598	13.424	5.779	9.513
24	20.00	2.7163	23.755	12.034	14.472	8.654	13.790	5.620	10.490	32.284	16.130	14.164	10.564	13.495	6.116	9.266
25	20.00	2.8192	13.181	6.986	17.440	6.436	17.241	5.357	12.260	22.642	11.501	17.092	9.459	16.842	6.084	11.897
26	20.00	2.9088	8.333	4.689	15.672	4.365	15.254	3.856	14.437	14.213	7.477	14.875	6.197	14.492	4.825	13.480
27	20.00	2.9939	10.861	5.885	14.095	5.020	13.418	3.981	12.039	17.227	8.913	13.401	6.744	12.733	4.717	11.273
28	20.00	3.0828	26.315	13.261	11.691	8.519	10.992	5.153	10.178	81.139	39.808	11.016	16.928	10.444	7.207	9.754

Note. This table is available entirely in machine-readable form for 1567 stellar models. Only model sequences of 20 $M_\odot$ stars are presented here. The initial physical properties of these stars are listed by H. Ge et al. (2020a).

(This table is available in its entirety in machine-readable form in the online article.)

11. $\tilde{\zeta}_{\rm ad}^{1}$— critical radius-mass exponent for conservative dynamical-timescale mass transfer,
12. $\tilde{q}_{\rm ad}^{1}$—critical initial mass ratio for conservative dynamical-timescale mass transfer,
13. $\tilde{M}_{\rm KH}^{1}$—mass threshold at which $\dot{M} = -M_{\rm i}/t_{\rm KH}$ and the tangent point for the minimum $q_{\rm ad}^{1}$,
14. $\tilde{q}_{\rm ad}^{0.5}$—critical initial mass ratio for semiconservative dynamical-timescale mass transfer,
15. $\tilde{M}_{\rm KH}^{0.5}$—mass threshold at which $\dot{M} = -M_{\rm i}/t_{\rm KH}$ and the tangent point for the minimum $q_{\rm ad}^{0.5}$,
16. $\tilde{q}_{\rm ad}^{0}$—critical initial mass ratio for fully nonconservative dynamical-timescale mass transfer, and
17. $\tilde{M}_{\rm KH}^{0}$—mass threshold at which $\dot{M} = -M_{\rm i}/t_{\rm KH}$ and the tangent point for the minimum $q_{\rm ad}^{0}$.

Finally, we complement the thresholds for nonconservative unstable mass transfer in $Z = 0.02$ stars in Table A4. Variables are the same as in Table A3. The full model grids cover 1567 ($Z = 0.02$) donors with masses from 0.1 to 100 $M_{\odot}$. H. Ge et al. (2020a) documented these donor stars' corresponding initial physical parameters in their tables 1 and 2.

ORCID iDs

Hongwei Ge https://orcid.org/0000-0002-6398-0195
Christopher A. Tout https://orcid.org/0000-0002-1556-9449
Xuefei Chen https://orcid.org/0000-0001-5284-8001
Song Wang https://orcid.org/0000-0003-3116-5038
Jianping Xiong https://orcid.org/0000-0003-4829-6245
Lifu Zhang https://orcid.org/0009-0001-3638-3133
Zhenwei Li https://orcid.org/0000-0002-1421-4427
Zhanwen Han https://orcid.org/0000-0001-9204-7778

References

Amaro-Seoane, P., Andrews, J., Arca Sedda, M., et al. 2023, LRR, 26, 2
Amaro-Seoane, P., Audley, H., Babak, S., et al. 2017, arXiv:1702.00786
Antokhin, I. I., Cherepashchuk, A. M., Antokhina, E. A., & Tatarnikov, A. M. 2022, ApJ, 926, 123
Antoniou, V., & Zezas, A. 2016, MNRAS, 459, 528
Ardern-Arentsen, A., Monari, G., Queiroz, A. B. A., et al. 2024, MNRAS, 530, 3391
Asplund, M., Grevesse, N., Sauval, A. J., & Scott, P. 2009, ARA&A, 47, 481
Barsukova, E. A., Borisov, N. V., Burenkov, A. N., et al. 2006, in ASP Conf. Ser. 355, Stars with the B[e] Phenomenon, ed. M. Kraus & A. S. Miroshnichenko (San Francisco, CA: ASP), 305
Bartlett, E. S., Clark, J. S., & Negueruela, I. 2019, A&A, 622, A93
Baykal, A., Stark, M. J., & Swank, J. 2000, ApJL, 544, L129
Belczynski, K., & Ziolkowski, J. 2009, ApJ, 707, 870
Bikmaev, I. F., Nikolaeva, E. A., Shimansky, V. V., et al. 2017, AstL, 43, 664
Bissinger, M. 2016, PhD thesis, Friedrich Alexander Univ. of Erlangen-Nuremberg, Germany
Bodaghee, A., Tomsick, J. A., Rodriguez, J., et al. 2011, ApJ, 727, 59
Boon, C. M., Bird, A. J., Hill, A. B., et al. 2016, MNRAS, 456, 4111
Bouchet, T., Chaty, S., Fortin, F., & Tomsick, J. A. 2022, MNRAS, 517, 3034
Butler, S. C., Tomsick, J. A., Chaty, S., et al. 2009, ApJ, 698, 502
Casares, J., Negueruela, I., Ribó, M., et al. 2014, Natur, 505, 378
Casares, J., Ribas, I., Paredes, J. M., Martí, J., & Allende Prieto, C. 2005a, MNRAS, 360, 1105
Casares, J., Ribó, M., Ribas, I., et al. 2005b, MNRAS, 364, 899
Casares, J., Ribo, M., Ribas, I., et al. 2012, MNRAS, 421, 1103
Chaty, S., & Rahoui, F. 2012, ApJ, 751, 150
Chaty, S., Rahoui, F., Foellmi, C., et al. 2008, A&A, 484, 783
Chen, X., Liu, Z., & Han, Z. 2024, PrPNP, 134, 104083
Chen, Z., & Ivanova, N. 2024, ApJL, 963, L35
Clark, J. S., Tarasov, A. E., Okazaki, A. T., Roche, P., & Lyuty, V. M. 2001, A&A, 380, 615
Coe, M. J., Bird, A. J., Hill, A. B., et al. 2007, MNRAS, 378, 1427
Coe, M. J., & Orosz, J. A. 2000, MNRAS, 311, 169
Coley, J. B., Corbet, R. H. D., & Krimm, H. A. 2015, ApJ, 808, 140
Conti, P. S., Crowther, P. A., & Leitherer, C. 2008, From Luminous Hot Stars to Starburst Galaxies (Cambridge: Cambridge Univ. Press)
Corbet, R. H. D., Chomiuk, L., Coe, M. J., et al. 2019, ApJ, 884, 93
Corbet, R. H. D., in't Zand, J. J. M., Levine, A. M., & Marshall, F. E. 2009, ApJ, 695, 30
Cox, N. L. J., Kaper, L., & Mokiem, M. R. 2005, A&A, 436, 661
Cusumano, G., D'Aì, A., Segreto, A., La Parola, V., & Del Santo, M. 2020, MNRAS, 498, 2750
Cusumano, G., La Parola, V., Segreto, A., & D'Aì, A. 2016, MNRAS, 456, 2717
Cusumano, G., Segreto, A., La Parola, V., et al. 2013, MNRAS, 436, L74
D'Aì, A., La Parola, V., Cusumano, G., et al. 2011, A&A, 529, A30
Doroshenko, V., Tsygankov, S., & Santangelo, A. 2018, A&A, 613, A19
Drave, S. P., Bird, A. J., Townsend, L. J., et al. 2012, A&A, 539, A21
Drave, S. P., Clark, D. J., Bird, A. J., et al. 2010, MNRAS, 409, 1220
Eggleton, P. P. 1971, MNRAS, 151, 351
Eggleton, P. P. 1983, ApJ, 268, 368
Falanga, M., Bozzo, E., Lutovinov, A., et al. 2015, A&A, 577, A130
Farrell, S. A., Sood, R. K., O'Neill, P. M., & Dieters, S. 2008, MNRAS, 389, 608
Ferrigno, C., Segreto, A., Mineo, T., Santangelo, A., & Staubert, R. 2008, A&A, 479, 533
Finger, M. H., Bildsten, L., Chakrabarty, D., et al. 1999, ApJ, 517, 449
Finger, M. H., Wilson, R. B., & Chakrabarty, D. 1996, A&AS, 120, 209
Flannery, B. P., & van den Heuvel, E. P. J. 1975, A&A, 39, 61
Fornasini, F., Antoniou, V., & Dubus, G. 2023, in Handbook of X-ray and Gamma-ray Astrophysics, ed. C. Bambi & A. Santangelo (Singapore: Springer), 143
Fortin, F., Chaty, S., & Sander, A. 2020, ApJ, 894, 86
Fortin, F., García, F., Simaz Bunzel, A., & Chaty, S. 2023, A&A, 671, A149
Gallegos-Garcia, M., Berry, C. P. L., & Kalogera, V. 2023, ApJ, 955, 133
Galloway, D. K., Morgan, E. H., & Levine, A. M. 2004, ApJ, 613, 1164
Galloway, D. K., Wang, Z., & Morgan, E. H. 2005, ApJ, 635, 1217
Ge, H., Hjellming, M. S., Webbink, R. F., Chen, X., & Han, Z. 2010, ApJ, 717, 724
Ge, H., Tout, C. A., Chen, X., et al. 2022, ApJ, 933, 137
Ge, H., Tout, C. A., Chen, X., et al. 2023, ApJ, 945, 7
Ge, H., Tout, C. A., Webbink, R. F., et al. 2024, ApJ, 961, 202
Ge, H., Webbink, R. F., Chen, X., & Han, Z. 2015, ApJ, 812, 40
Ge, H., Webbink, R. F., Chen, X., & Han, Z. 2020a, ApJ, 899, 132
Ge, H., Webbink, R. F., & Han, Z. 2020b, ApJS, 249, 9
Gomez, S., & Grindlay, J. E. 2021, ApJ, 913, 48
Goossens, M. E., Bird, A. J., Drave, S. P., et al. 2013, MNRAS, 434, 2182
Götz, D., Falanga, M., Senziani, F., et al. 2007, ApJL, 655, L101
Haberl, F., & Sturm, R. 2016, A&A, 586, A81
Hainich, R., Oskinova, L. M., Torrejón, J. M., et al. 2020, A&A, 634, A49
Harmanec, P., Habuda, P., Štefl, S., et al. 2000, A&A, 364, L85
Heida, M., Lau, R. M., Davies, B., et al. 2019, ApJL, 883, L34
Hills, J. G. 1983, ApJ, 267, 322
Hinkle, K. H., Lebzelter, T., Fekel, F. C., et al. 2020, ApJ, 904, 143
Hjellming, M. S., & Webbink, R. F. 1987, ApJ, 318, 794
Hurley, J. R., Tout, C. A., & Pols, O. R. 2002, MNRAS, 329, 897
in't Zand, J. J. M., Corbet, R. H. D., & Marshall, F. E. 2001, ApJL, 553, L165
in't Zand, J. J. M., Kuiper, L., den Hartog, P. R., Hermsen, W., & Corbet, R. H. D. 2007, A&A, 469, 1063
Jeon, M., Pawlik, A. H., Bromm, V., & Milosavljević, M. 2014, MNRAS, 440, 3778
Jonker, P. G., Nelemans, G., & Bassa, C. G. 2007, MNRAS, 374, 999
Kaaret, P., Cusumano, G., & Sacco, B. 2000, ApJL, 542, L41
Kaper, L., van der Meer, A., van Kerkwijk, M., & van den Heuvel, E. 2006, Msngr, 126, 27
Kim, V., Izmailova, I., & Aimuratov, Y. 2023, ApJS, 268, 21
King, A., Lasota, J.-P., & Middleton, M. 2023, NewAR, 96, 101672
Klencki, J., Istrate, A., Nelemans, G., & Pols, O. 2022, A&A, 662, A56
Koh, D. T., Bildsten, L., Chakrabarty, D., et al. 1997, ApJ, 479, 933
Koyama, K., Kawada, M., Tawara, Y., et al. 1991, ApJL, 366, L19
Kretschmar, P., El Mellah, I., Martínez-Núñez, S., et al. 2021, A&A, 652, A95
Krtička, J., Kubát, J., & Krtičková, I. 2015, A&A, 579, A111
La Parola, V., Cusumano, G., Romano, P., et al. 2010, MNRAS, 405, L66
Lehmer, B. D., Eufrasio, R. T., Basu-Zych, A., et al. 2021, ApJ, 907, 17
Li, H., Tan, K., & Zhao, G. 2018, ApJS, 238, 16
Li, Z., & Chen, X. 2024, ResPh, 59, 107568
Li, Z., Chen, X., Ge, H., Chen, H.-L., & Han, Z. 2023, A&A, 669, A82

Liao, Z., Liu, J., Zheng, X., & Gou, L. 2020, MNRAS, 492, 5922
Liu, Q. Z., van Paradijs, J., & van den Heuvel, E. P. J. 2006, A&A, 455, 1165
Liu, Z.-W., Röpke, F. K., & Han, Z. 2023, RAA, 23, 082001
Luo, J., Chen, L.-S., Duan, H.-Z., et al. 2016, CQGra, 33, 035010
Maitra, C., & Paul, B. 2013, ApJ, 771, 96
Malacaria, C., Heyl, J., Doroshenko, V., et al. 2023, A&A, 675, A29
Mandel, I., & Broekgaarden, F. S. 2022, LRR, 25, 1
Mandel, I., Müller, B., Riley, J., et al. 2021, MNRAS, 500, 1380
Martínez-Núñez, S., Sander, A., Gímenez-García, A., et al. 2015, A&A, 578, A107
Masetti, N., Pretorius, M. L., Palazzi, E., et al. 2006, A&A, 449, 1139
Mason, A. B., Clark, J. S., Norton, A. J., Negueruela, I., & Roche, P. 2009, A&A, 505, 281
Massey, P., Neugent, K. F., & Morrell, N. 2017, ApJ, 837, 122
Meynet, G., & Maeder, A. 2003, A&A, 404, 975
Meynet, G., & Maeder, A. 2005, A&A, 429, 581
Miller-Jones, J. C. A., Bahramian, A., Orosz, J. A., et al. 2021, Sci, 371, 1046
Misra, D., Fragos, T., Tauris, T. M., Zapartas, E., & Aguilera-Dena, D. R. 2020, A&A, 642, A174
Mokiem, M. R., de Koter, A., Evans, C. J., et al. 2007, A&A, 465, 1003
Moritani, Y., Kawano, T., Chimasu, S., et al. 2018, PASJ, 70, 61
Motch, C., Haberl, F., Dennerl, K., Pakull, M., & Janot-Pacheco, E. 1997, A&A, 323, 853
Motch, C., Pakull, M. W., Grisé, F., & Soria, R. 2011, AN, 332, 367
Motch, C., Pakull, M. W., Soria, R., Grisé, F., & Pietrzyński, G. 2014, Natur, 514, 198
Müller, S., Ferrigno, C., Kühnel, M., et al. 2013, A&A, 551, A6
Nabizadeh, A., Tsygankov, S. S., Molkov, S. V., et al. 2022, A&A, 657, A58
Negueruela, I., Israel, G. L., Marco, A., Norton, A. J., & Speziali, R. 2003, A&A, 397, 739
Negueruela, I., & Okazaki, A. T. 2001, A&A, 369, 108
Negueruela, I., Ribó, M., Herrero, A., et al. 2011, ApJL, 732, L11
Neijssel, C. J., Vigna-Gómez, A., Stevenson, S., et al. 2019, MNRAS, 490, 3740
Neumann, M., Avakyan, A., Doroshenko, V., & Santangelo, A. 2023, A&A, 677, A134
Nikolaeva, E. A., Bikmaev, I. F., Melnikov, S. S., et al. 2013, BCrAO, 109, 27
Orosz, J. A., Kuulkers, E., van der Klis, M., et al. 2001, ApJ, 555, 489
Paczynski, B. 1976, in IAU Symp. 73, Structure and Evolution of Close Binary Systems, ed. P. Eggleton, S. Mitton, & J. Whelan (Cambridge: Cambridge Univ. Press), 75
Pellizza, L. J., Chaty, S., & Negueruela, I. 2006, A&A, 455, 653
Picchi, P., Shore, S. N., Harvey, E. J., & Berdyugin, A. 2020, A&A, 640, A96
Pols, O. R., Tout, C. A., Eggleton, P. P., & Han, Z. 1995, MNRAS, 274, 964
Prat, L., Rodriguez, J., Hannikainen, D. C., & Shaw, S. E. 2008, MNRAS, 389, 301
Preston, G. W., & Sneden, C. 2000, AJ, 120, 1014
Raichur, H., & Paul, B. 2010, MNRAS, 406, 2663
Reig, P., Chakrabarty, D., Coe, M. J., et al. 1996, A&A, 311, 879
Reig, P., Fabregat, J., & Alfonso-Garzón, J. 2020, A&A, 640, A35
Reig, P., Fabregat, J., Coe, M. J., et al. 1997, A&A, 322, 183
Reig, P., Negueruela, I., Buckley, D. A. H., et al. 2001, A&A, 367, 266
Reig, P., Negueruela, I., Fabregat, J., et al. 2004, A&A, 421, 673
Reig, P., Tzouvanou, A., Blinov, D., & Pantoulas, V. 2023, A&A, 671, A48
Reynolds, A. P., Bell, S. A., & Hilditch, R. W. 1992, MNRAS, 256, 631
Ribó, M., Negueruela, I., Blay, P., Torrejón, J. M., & Reig, P. 2006, A&A, 449, 687
Richardson, N. D., Pavao, C. M., Eldridge, J. J., et al. 2023, Natur, 614, 45
Rodríguez Castillo, G. A., Israel, G. L., Belfiore, A., et al. 2020, ApJ, 895, 60
Romano, P., Bozzo, E., Mangano, V., et al. 2015, A&A, 576, L4
Romano, P., Sidoli, L., Ducci, L., et al. 2010, MNRAS, 401, 1564
Saavedra, E. A., Fogantini, F. A., Escobar, G. J., et al. 2023, A&A, 680, A88
Salganik, A., Tsygankov, S. S., Djupvik, A. A., et al. 2022, MNRAS, 509, 5955
Sandage, A. R. 1953, AJ, 58, 61
Schaller, G., Schaerer, D., Meynet, G., & Maeder, A. 1992, A&AS, 96, 269
Scherbak, P., & Fuller, J. 2023, MNRAS, 518, 3966
Schulz, N. S., Kallman, T. E., Heinz, S., et al. 2020, ApJ, 891, 150
Sguera, V., Drave, S. P., Bird, A. J., et al. 2011, MNRAS, 417, 573
Sharma, R., Jain, C., Rikame, K., & Paul, B. 2023, MNRAS, 519, 1764
Sierpowska-Bartosik, A., & Bednarek, W. 2008, MNRAS, 385, 2279
Smartt, S. J., Maund, J. R., Hendry, M. A., et al. 2004, Sci, 303, 499
Staubert, R., Trümper, J., Kendziorra, E., et al. 2019, A&A, 622, A61
Stevens, J. B., Reig, P., Coe, M. J., et al. 1997, MNRAS, 288, 988
Stollberg, M. T., Finger, M. H., Wilson, R. B., et al. 1999, ApJ, 512, 313
Tauris, T. M., & van den Heuvel, E. P. J. 2023, Physics of Binary Star Evolution. From Stars to X-ray Binaries and Gravitational Wave Sources (Princeton, NJ: Princeton Univ. Press)
Torrejón, J. M., Negueruela, I., Smith, D. M., & Harrison, T. E. 2010, A&A, 510, A61
Tutukov, A., & Yungelson, L. 1973, NInfo, 27, 70
Uchida, N., Takahashi, H., Fukazawa, Y., & Makishima, K. 2021, PASJ, 73, 1389
van den Heuvel, E. P. J., & Heise, J. 1972, NPhS, 239, 67
van Soelen, B., Mc Keague, S., Malyshev, D., et al. 2022, MNRAS, 515, 1078
Vink, J. S., Higgins, E. R., Sander, A. A. C., & Sabhahit, G. N. 2021, MNRAS, 504, 146
Webbink, R. F. 1984, ApJ, 277, 355
Webbink, R. F. 1985, in Interacting Binary Stars, ed. J. E. Pringle & R. A. Wade (Cambridge: Cambridge Univ. Press), 39
Willcox, R., MacLeod, M., Mandel, I., & Hirai, R. 2023, ApJ, 958, 138
Wilson, C. A., Finger, M. H., Coe, M. J., & Negueruela, I. 2003, ApJ, 584, 996
Wilson, C. A., Finger, M. H., Harmon, B. A., et al. 1997, ApJ, 479, 388
Woosley, S. E. 1987, in IAU Symp. 125, The Origin and Evolution of Neutron Stars, ed. D. J. Helfand & J. H. Huang (Cambridge: Cambridge Univ. Press), 255
Wu, Y., Xiang, M., Chen, Y., et al. 2021, MNRAS, 501, 4917
Yamamoto, T., Mihara, T., Sugizaki, M., et al. 2014, PASJ, 66, 59
Yan, J., Zurita Heras, J. A., Chaty, S., Li, H., & Liu, Q. 2012, ApJ, 753, 73
Zampieri, L., & Roberts, T. P. 2009, MNRAS, 400, 677
Zhang, L., Ge, H., Chen, X., & Han, Z. 2024, ApJS, 274, 11
Zhao, Y., Gandhi, P., Dashwood Brown, C., et al. 2023, MNRAS, 525, 1498